THE ASTROPHYSICAL JOURNAL, 555:990–1012, 2001 July 10

SOLAR MODELS: CURRENT EPOCH AND TIME DEPENDENCES, NEUTRINOS, AND HELIOSEISMOLOGICAL PROPERTIES

JOHN N. BAHCALL
Institute for Advanced Study, Olden Lane, Princeton, NJ 08540
M. H. PINSONNEAULT
Department of Astronomy, Ohio State University, Columbus, OH 43210
AND
SARBANI BASU
Astronomy Department, Yale University, P.O. Box 208101, New Haven, CT 06520-8101
Received 2000 October 29; accepted 2001 March 12

ABSTRACT

We calculate accurate solar models and report the detailed time dependences of important solar quantities. We use helioseismology to constrain the luminosity evolution of the Sun and report the discovery of semiconvection in evolved solar models that include diffusion. In addition, we compare the computed sound speeds with the results of *p*-mode observations by BiSON, GOLF, GONG, LOWL, and MDI instruments. We contrast the neutrino predictions from a set of eight standard-like solar models and four deviant (or deficient) solar models with the results of solar neutrino experiments. For solar neutrino and helioseismological applications, we present present-epoch numerical tabulations of characteristics of the standard solar model as a function of solar radius, including the principal physical and composition variables, sound speeds, neutrino fluxes, and functions needed for calculating solar neutrino oscillations.

Subject headings: neutrinos — Sun: helioseismology — Sun: interior — Sun: particle emission
On-line material: color figures

1. INTRODUCTION

Why are new calculations of standard solar models of interest? After all, solar models have been used to calculate neutrino fluxes since 1962 (Bahcall et al. 1963), and solar atmospheres have been used to calculate *p*-mode oscillation frequencies since 1970 (Ulrich 1970; Leibacher & Stein 1971). Over the past four decades, the accuracy with which solar models are calculated has been steadily refined as the result of increased observational and experimental information about the input parameters (such as nuclear reaction rates and the surface of abundances of different elements), more accurate calculations of constituent quantities (such as radiative opacity and equation of state), the inclusion of new physical effects (such as element diffusion), and the development of faster computers and more precise stellar evolution codes.

Solar models nevertheless remain at the frontiers of two different scientific disciplines, solar neutrino studies and helioseismology. In an era in which many major laboratory studies are underway to study neutrino oscillations with the aid of very long baselines, $\sim 10^3$ km, between accelerator and detector, solar neutrinos have a natural advantage, with a baseline of 10^8 km (Pontecorvo 1968). In addition, solar neutrinos provide unique opportunities for studying the effects of matter upon neutrino propagation, the so-called MSW effect (Wolfenstein 1978; Mikheyev & Smirnov 1985), since on their way to terrestrial detectors they pass through large amounts of matter in the Sun and, at night, also in Earth.

The connection with ongoing solar neutrino research imposes special requirements on authors carrying out the most detailed solar modeling. Precision comparisons between neutrino measurements and solar predictions are used by many physicists to refine the determination of neutrino parameters and to test different models of neutrino propagation. Since the neutrino experiments and the associated analysis of solar neutrino data are refined at frequent intervals, it is appropriate to reevaluate and refine the solar model predictions as improvements are made in the model input parameters, calculational techniques, and descriptions of the microscopic and macroscopic physics.

In this paper we provide new information about the total solar neutrino fluxes and the predicted neutrino event rates for a set of standard and nonstandard solar models. Using the best available standard solar model, we also present the calculated radial dependence of the production rate for each of the important solar neutrino fluxes. We publish for the first time the results of a precision calculation with the standard solar model of the electron density throughout the Sun, from the innermost regions of the solar core to the solar atmosphere. We also present for the first time a detailed calculation of the radial profile of the number density of scatterers of sterile neutrinos. These quantities are important for precision studies of neutrino oscillations using solar neutrinos.

We also provide detailed predictions for the time evolution of some of the important solar characteristics such as the depth and mass of the solar convective zone; the radius and the luminosity of the Sun; the central temperature, density, pressure, and hydrogen mass fraction; as well as the temperature, density, pressure, and radiative opacity at the base of the convective zone. As far as we know, these are the first detailed results submitted for publication on the time evolution of many of these quantities. Some of the calculated time dependences may be subject to observational tests.

At the present writing, the Sun remains the only main-sequence star for which *p*-mode oscillations have been robustly detected. Thus, only for the Sun can one measure precisely tens of thousands of the eigenfrequencies for

stellar pressure oscillations. The comparison between the sound speeds and pressures derived from the observed *p*-mode frequencies and those calculated with standard solar models has provided a host of accurate measurements of the interior of the nearest star. The solar quantities determined by helioseismology include the sound velocity and density as a function of solar radius, the depth of the convective zone, the interior rotation rate, and the surface helium abundance. The excellent agreement between the helioseismological observations and the solar model calculations has shown that the large discrepancies between solar neutrino measurements and solar model calculations cannot be due to errors in the solar models (see Fig. 11 below).

In this paper we present a refined comparison between our best standard solar model and measurements of the solar sound speeds obtained using oscillation data from a number of different sources. We use a combination of data from the LOWL instrument and the BiSON network, two sets of data from the GOLF instrument, as well as data from the GONG network and the MDI instrument.

We describe in the following paragraph the organization of this paper. However, since this paper contains a lot of information on disparate topics, we recommend that the reader first turn to § 8 and peruse our summary and discussion of the main new results. Section 8 may help the reader decide which sections of the paper he/she wants to read (or skip). The different sections are written so that they can be read more or less independently.

Section 2 defines the slightly improved standard solar model and describes the numerical tables that present details of the contemporary characteristics of the standard model. Section 3 describes the main-sequence time dependences of some of the most important characteristics of the standard model. We present in this section the time evolution of the solar radius and luminosity, the properties of the convective zone, and the physical characteristics of the center of the Sun. We discuss solar properties from the initial-age main sequence to an age of 8×10^9 yr. Section 4 defines and compares the physical characteristics of seven variant standard models and four deviant (deficient) solar models, which together with the standard model make up a set of 12 models whose neutrino fluxes we evaluate in this paper. We previously used a subset of nine of these models to test the robustness of helioseismological inversions (Basu, Pinsonneault, & Bahcall 2000, hereafter BPB00). We discuss in this same section two new standard-like solar models with heavy-element–to–hydrogen ratios that differ slightly from our previously adopted value of Z/X. Section 5 discusses solar neutrino physics. We present the predicted present-day neutrino fluxes for the standard model and for all of the variant and deviant solar models, as well as the electron number density versus solar radius. We contrast the predicted neutrino event rates with the results of the chlorine, Kamiokande, GALLEX, SAGE, Super-Kamiokande, and GNO solar neutrino experiments. We also give in this section the calculated time evolution of the most important solar neutrino fluxes. Section 6 compares calculated and observed sound speeds. We present the results both on a panoramic scale suitable for discussing the implications for solar neutrino physics and on a zoomed-in scale appropriate for detailed investigations of solar physics. In § 7 we compare, for all 12 of the solar models discussed in this paper, the calculated values of the surface helium abundance and the depth of the convective zone with the measured values for these quantities. We summarize and discuss our main results in § 8.

The interested reader may wish to consult the following works that summarize the solar neutrino aspects of solar models (Bahcall 1989; Bahcall & Pinsonneault 1992, 1995; Berezinsky, Fiorentini, & Lissia 1996; Castellani et al. 1997; Richard et al. 1996; Turck-Chièze et al. 1993; Bahcall, Basu, & Pinsonneault 1998, hereafter BBP98) and the helioseismologic aspects of solar models (Bahcall & Ulrich 1988; Bahcall & Pinsonneault 1995; Christensen-Dalsgaard et al. 1996; Guenther & Demarque 1997; Guzik 1998; Turck-Chièze et al. 1998; Brun, Turck-Chièze, & Zahn 1999; Ricci & Fiorentini 2000).

2. STANDARD SOLAR MODEL

We define in § 2.1 the standard solar model and present in § 2.2 some of the important contemporary characteristics of the standard solar model, including detailed tables of the physical variables as a function of the solar radius.

By "the standard solar model," we mean the solar model that is constructed with the best available physics and input data. All of the solar models we consider, standard or "deviant" models (see below), are required to fit the observed luminosity and radius of the Sun at the present epoch, as well as the observed heavy-element–to–hydrogen ratio at the surface of the Sun. No helioseismological constraints are used in defining the standard solar model.

Naturally, standard models improve with time, as the input data are made more accurate, the calculational techniques become faster and more precise, and the physical description is more detailed. Thus, it is necessary at each presentation of a new standard model to describe what has changed from the previous best model and to provide references to the earlier work. The reader can see Bahcall (1989) for a general reference to the early work on precise solar models that were motivated by the need to predict accurate solar neutrino fluxes and to make comparisons with helioseismological data.

2.1. *Definition of the Standard Model*

Our standard solar model[1] is constructed with the OPAL equation of state (Rogers, Swenson, & Iglesias 1996) and OPAL opacities (Iglesias & Rogers 1996), which are supplemented by the low-temperature opacities of Alexander & Ferguson (1994). The model was calculated using the usual mixing length formalism to determine the convective flux.

The principal change in the input data is the use of the Grevesse & Sauval (1998) improved standard solar composition in the OPAL opacities[2] and in the calculation of the nuclear reaction rates. The refinements in this composition redetermination come from many different sources, including the use of more accurate atomic transition probabilities in interpreting solar spectra. The OPAL equation of state and the Alexander and Ferguson opacities are not yet available with the composition recommended by Grevesse & Sauval (1998).

[1] To simplify the language of the discussion, we will often describe characteristics of the standard model as if we knew they were characteristics of the Sun. We will sometimes abbreviate the reference to this standard model as BP2000.

[2] See http://www-phys.llnl.gov/Research/OPAL/index.html.

We have used a present-epoch solar luminosity of 1369 W m^2[4π(AU)^2] for all the models described in detail in this paper. Only for the neutrino fluxes presented in §§ 5.1.1 and 5.1.3 have we used the more recent best estimate value of solar luminosity, 1366.2 W m^2[4π(AU)^2] = 3.842×10^{33} ergs^{-1} (see Fröhlich & Lean 1998; Crommelynck et al. 1996). The difference between these two values for the luminosity is 0.2%. For the calculations of uncertainties in neutrino flux predictions, we assume a 1 σ uncertainty of 0.4%. The uncertainty in the predicted solar neutrino fluxes due to the luminosity is an order of magnitude smaller than the total uncertainty in predicting the neutrino fluxes. For all the other quantities we calculate, the uncertainty in the solar luminosity has an even smaller effect.

The nuclear reaction rates were evaluated with the subroutine exportenergy.f (see Bahcall & Pinsonneault 1992), using the reaction data in Adelberger et al. (1998) and with electron and ion weak screening as indicated by recent calculations of Gruzinov & Bahcall (1998; see also Salpeter 1954).[3] The model incorporates helium and heavy-element diffusion using the exportable diffusion subroutine of Thoul (see Thoul, Bahcall, & Loeb 1994; Bahcall & Pinsonneault 1995).[4] An independent and detailed treatment of diffusion by Turcotte et al. (1998) yields results for the impact of diffusion on the computed solar quantities that are very similar to those obtained here. We have used the most recent and detailed calculation (Marcucci et al. 2000a) for the S_0-factor for the ^{3}He(p, $e^+ + \nu_e$)^{4}He reaction: $S_0(hep) = 10.1 \times 10^{-20}$ keV b, which is a factor of 4.4 times larger than the previous best estimate [for a discussion of the large uncertainties in calculating $S_0(hep)$ see § 5.1.2; Bahcall & Krastev 1998; Marcucci et al. 2000b]. For values of $S_0(hep)$ in the range of current estimates, the assumed rate of the *hep*-reaction only affects in a noticeable way the calculated flux of *hep* neutrinos and does not affect the calculated fluxes of other neutrinos, the helioseismological characteristics, or other physical properties of the Sun.

For the standard model, the evolutionary calculations were started at the main-sequence stage. The model has a radius of 695.98 Mm. We do not study the pre–main-sequence evolution in our standard model. This epoch has been discussed in the classical work of Iben (1965), and the effects of pre–main sequence have been shown by Bahcall & Glasner (1994) to be unimportant for solar neutrino calculations (see also the thorough discussion by Morel, Provost, & Berthomieu 2000a). We do consider one pre–main-sequence model, which differs very little from the corresponding model started at the zero-age main sequence.

The ratio of heavy elements to hydrogen (Z/X) at the surface of the model is 0.0230, which was chosen to be consistent with the value obtained by Grevesse & Sauval (1998). A Krishna-Swamy T-τ relationship for the atmosphere was used. We adopt a solar luminosity $L_\odot = 3.844 \times 10^{33}$ ergs s^{-1} and a solar age of 4.57×10^9 yr (see Bahcall & Pinsonneault 1995).

In the course of our recent analysis of systematic uncertainties in helioseismological inversions (BPB00), we uncovered an error in the code we wrote for the interpolation of the OPAL 95 opacities. The edges of opacity tables were flagged by zero opacity values; unfortunately, there were some interpolation problems associated with the occurrence of zero values inside the table. This problem occurred because the logarithm of the opacity, which is what we were tabulating, can actually be zero. The interpolation error caused small changes in the opacity that produced errors in the sound speed of order 0.1% for solar radii in the range of 0.3–0.7 $R_\odot$ and errors of order 3% in the ^{8}B neutrino flux (with smaller errors for other neutrino fluxes). In the following sections, we will point out more specifically the changes in the neutrino predictions and in the sound velocities that are produced by correcting this interpolation error. These changes are particularly apparent in the comparison of Figures 13 and 14, which are discussed in the helioseismology section, § 6.

2.2. *Some Contemporary Characteristics of the Standard Solar Model*

The details of the structure of a standard solar model are of importance for both helioseismology and solar neutrino calculations. In the first paper in this series in which we published the details of a model of the solar interior structure (Bahcall et al. 1982), we presented a table with only 27 radial shells (rows of numbers) and 10 variables for each shell (mass, radius, temperature, density, hydrogen fraction, helium fraction, luminosity generated, and the source density of the *p-p*, ^{7}Be, and ^{8}B neutrinos). Over the years, much greater precision was required by the increasing sophistication of the helioseismological measurements and the solar neutrino calculations. Fortunately, the computing capacity more than made up for the necessary increase in model details.

We have created from the output of the present calculations two exportable computer files that contain in easily readable form the details of our best standard solar model (BP2000). Physical variables are given at 875 separate radial shells, which is the same number of shells used to calculate the solar interior model. In addition to the variables cited above, this file contains the pressure, electron number density, the mass fractions of ^{3}He, ^{7}Be, ^{12}C, ^{14}N, and ^{16}O, and the source densities of all eight of the most important solar neutrino fluxes. These files are accessible on-line (see footnote 4 for the URL). Previous standard solar models in this series (published in 1982, 1988, 1992, 1995, and 1998) are available at the same URL and can be used to test the robustness of conclusions that depend upon models of the solar interior.

3. TIME DEPENDENCES

In this section we present and discuss the time dependences of some of the principal characteristics of the standard solar model. We begin in § 3.1 by describing the separate temporal evolution of the solar radius and the solar luminosity and then discuss the simple relation we have found between the values of these two quantities as a function of time. We also demonstrate that the solar luminosity is a robust function of time. In § 3.2 we present the

[3] Other approximations to screening are sometimes used. The numerical procedures of Dzitko et al. (1995) and Mitler (1977) predict reaction rates that are too slow for heavy ions because they assumed that the electron charge density near a screened nucleus is the unperturbed value, $en_e(\infty)$. This assumption seriously underestimates the charge density near heavy ions. For example, it is known that a screened beryllium nucleus under solar interior conditions has charge density near the nucleus $\approx -3.85en_e(\infty)$ (Gruzinov & Bahcall 1997; Brown & Sawyer 1997; all quantum mechanical calculations give similar results; see Bahcall 1962; Iben, Kalata, & Schwartz 1967).

[4] Both the nuclear energy generation subroutine, exportenergy.f, and the diffusion subroutine, diffusion.f, are available at http://www.sns.ias.edu/~jnb, under menu item "software and data."

time-dependent fractions of the solar luminosity that are produced by different nuclear fusion reactions. We concentrate in § 3.3 on the convective zone, presenting the calculated time dependences of the depth and the mass of the convective zone. We also report the time dependence of the temperature, density, pressure, and opacity at the base of the convective zone. In § 3.4 we discuss the time dependence of quantities at the center of the Sun, the central temperature, density, pressure, and hydrogen mass fraction. In § 3.5 we calculate and discuss the large and small separations of the *p*-mode frequencies as a function of solar age. Since we do not discuss pre–main-sequence evolution, our calculations are not precise for times less than 0.1×10^9 yr (see Morel et al. 2000a; Weiss & Schlattl 1998).

Iben (1967, 1974) and Demarque & Guenther (1991) summarize in comprehensive presentations the evolution of solar parameters in models that were calculated prior to the inclusion of element diffusion in solar evolutionary codes. These discussions did not encounter the problem of semiconvection discussed here in § 3.3 because this phenomenon is caused by effects of diffusion near the base of the convective zone.

The solar radius and luminosity (or equivalently, the solar effective temperature and luminosity) constitute precise constraints on the possible geological histories of Earth. We quantify these constraints in the following subsection and specify upper limits to the allowed discrepancies from the standard solar model profile of solar luminosity versus age.

3.1. *Radius and Luminosity versus Age*

Figure 1 and Table 1 present the calculated radius of the Sun versus solar age for the standard solar model. The values given are normalized to the present-day solar radius, $R_\odot$. Over the lifetime of the Sun, the model radius has increased monotonically from an initial value of 0.869 $R_\odot$ to the current value 1.0 $R_\odot$, a 15% rise. At a solar age of 8×10^9 yr, the solar radius will increase to 1.17 $R_\odot$. We shall see in the following discussion that some of the important evolutionary characteristics of the Sun can be expressed simply in terms of the ratio $R_\odot(t)/R_\odot$(today).

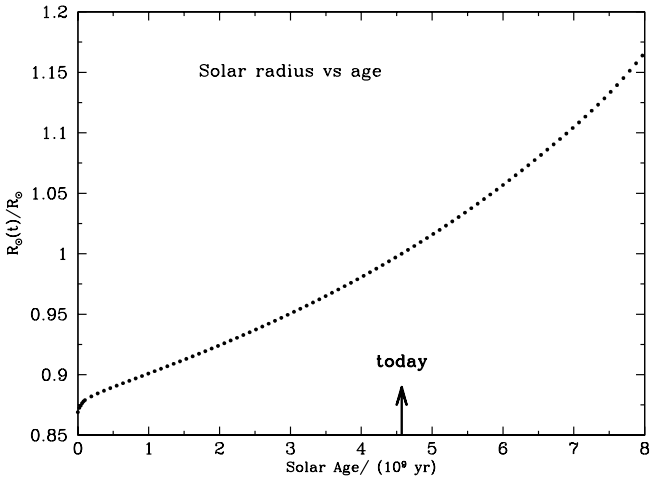

FIG. 1.—Calculated radius, $R_\odot(t)$, as a function of age for the standard solar model, BP2000. The solar age is measured in units of 10^9 yr. The present age of the Sun, 4.57×10^9 yr, is indicated by an arrow. The radius increases from 0.87 $R_\odot$ at the zero-age main sequence to 1.0 $R_\odot$ at the present epoch and 1.18 $R_\odot$ at a solar age of 8×10^9 yr. [*See the electronic edition of the Journal for a color version of this figure.*]

TABLE 1

SOLAR RADIUS, $R_\odot(t)$, AS A FUNCTION OF SOLAR AGE FOR THE STANDARD SOLAR MODEL

Age (10^9 yr)	$R_\odot(t)$ [$R_\odot$(today)]	Age (10^9 yr)	$R_\odot(t)$ [$R_\odot$ (today)]
0.0.....	0.869	4.2.....	0.987
0.2.....	0.882	4.4.....	0.994
0.4.....	0.888	4.6.....	1.001
0.6.....	0.892	4.8.....	1.008
0.8.....	0.897	5.0.....	1.016
1.0.....	0.901	5.2.....	1.023
1.2.....	0.906	5.4.....	1.031
1.4.....	0.910	5.6.....	1.040
1.6.....	0.915	5.8.....	1.048
1.8.....	0.920	6.0.....	1.057
2.0.....	0.924	6.2.....	1.066
2.2.....	0.929	6.4.....	1.075
2.4.....	0.934	6.6.....	1.085
2.6.....	0.940	6.8.....	1.095
2.8.....	0.945	7.0.....	1.105
3.0.....	0.951	7.2.....	1.116
3.2.....	0.956	7.4.....	1.127
3.4.....	0.962	7.6.....	1.139
3.6.....	0.968	7.8.....	1.152
3.8.....	0.974	8.0.....	1.166
4.0.....	0.981	...	...

NOTE.—The present age of the Sun is 4.57×10^9 yr (see Bahcall & Pinsonneault 1995).

Figure 2 and Table 2 show the calculated solar luminosity as a function of solar age, normalized to the present-day solar luminosity, $L_\odot$. For the standard model, the total

TABLE 2

SOLAR LUMINOSITY AS A FUNCTION OF SOLAR AGE FOR THE STANDARD SOLAR MODEL

Age (10^9 yr)	$L_\odot(t)$ [$L_\odot$ (today)]	Age (10^9 yr)	$L_\odot(t)$ [$L_\odot$ (today)]
0.0.....	0.677	4.2.....	0.970
0.2.....	0.721	4.4.....	0.986
0.4.....	0.733	4.6.....	1.003
0.6.....	0.744	4.8.....	1.020
0.8.....	0.754	5.0.....	1.037
1.0.....	0.764	5.2.....	1.055
1.2.....	0.775	5.4.....	1.073
1.4.....	0.786	5.6.....	1.092
1.6.....	0.797	5.8.....	1.112
1.8.....	0.808	6.0.....	1.132
2.0.....	0.820	6.2.....	1.152
2.2.....	0.831	6.4.....	1.172
2.4.....	0.844	6.6.....	1.193
2.6.....	0.856	6.8.....	1.214
2.8.....	0.869	7.0.....	1.235
3.0.....	0.882	7.2.....	1.256
3.2.....	0.896	7.4.....	1.278
3.4.....	0.910	7.6.....	1.304
3.6.....	0.924	7.8.....	1.332
3.8.....	0.939	8.0.....	1.363
4.0.....	0.954	...	...

NOTE.—The table gives the computed values of the solar luminosity in units of the present-day solar luminosity. The model was iterated to give the observed luminosity at the present epoch, 4.57×10^9 yr.

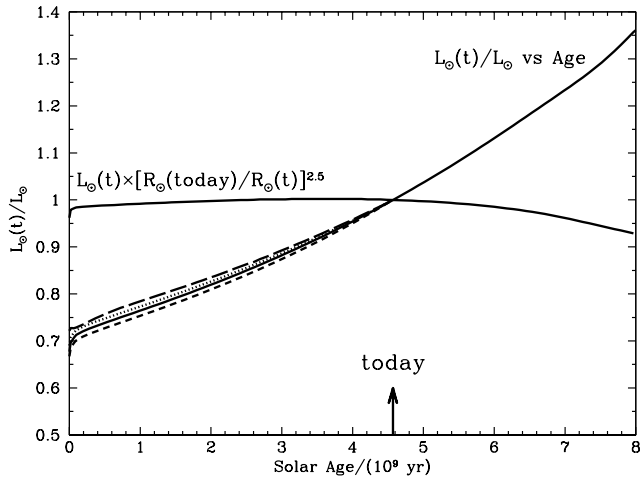

FIG. 2.—Normalized solar luminosity, $L_\odot(t)/L_\odot(\text{today})$, vs. solar age for the standard solar model (*solid curve*) and for three "deficient" solar models: the No Diffusion model (*dotted curve*), the $S_{34} = 0$model (*short-dashed curve*), and the Mixed model (*long-dashed curve*). The luminosity evolution of the Sun is essentially the same in all solar models we have investigated, including deficient solar models. The rms deviation of the deviant models from the standard solar model luminosity is only 1% over the history of the Sun from the zero-age main sequence to the current epoch (see text for more details). The product $L_\odot(t)R_\odot(t)^{-2.5}$ varies by $\pm 4\%$ over the entire period from the zero-age main sequence to a solar age of 8×10^9 yr, while the solar luminosity itself varies by slightly more than a factor of 2 during this period. In the period between 4×10^9 and 8×10^9 yr, the relation $L_\odot(t) \propto R_\odot(t)^2$ is satisfied to $\pm 0.5\%$. The solar luminosity has increased by 48% from the zero-age main sequence to the present epoch. The present age of the Sun is indicated by an arrow at 4.59×10^9 yr. [*See the electronic edition of the Journal for a color version of this figure.*]

solar luminosity has risen monotonically from a zero-age value of 0.677 $L_\odot$.

The time evolution of the solar luminosity is robust. We also show in Figure 2 the solar luminosity as a function of time for the three most deficient solar models that are described in § 4. The rms difference between the standard luminosity and the luminosity of the deviant models is 1.6% for the mixed model (1.2% ignoring the first gigayear), 0.7% for the no-diffusion model (0.5% ignoring the first gigayear), and 0.9% for the $S_{34} = 0$ model (0.8% ignoring the first gigayear). The largest deviations occur for the zero-age main-sequence models and are 2.5% for the mixed model, 1.9% for the no-diffusion model, and 1.7% for the $S_{34} = 0$ model. All of the solar models show essentially the same shape for the luminosity evolution as a function of age.

Figure 2 shows that the product

$$L_\odot(t)[R_\odot(t)]^{-2.5} = \text{constant} \qquad (1)$$

to an accuracy of about $\pm 4\%$ over the entire period from the zero-age main sequence to an age of 8×10^9 yr. The solar luminosity $L_\odot(t)$ varies from 0.68 $L_\odot$ to $L_\odot$ at the present epoch and will reach 1.36 $L_\odot$ after 8×10^9 yr on the main sequence. The corresponding values of $L_\odot(t)[R_\odot(\text{today})/R_\odot(t)]^{2.5}$ are 0.96, 1.00, and 0.93. Thus, the luminosity of the Sun varies by slightly more than a factor of 2 while $L_\odot(t)[R_\odot(\text{today})/R_\odot(t)]^{2.5}$ varies by only a few percent.

Over the first 5×10^9 yr, equation (1) is satisfied to an accuracy of $\pm 2\%$. From 4×10^9 to 8×10^9 yr, the relation is somewhat less steep, $L_\odot(t) \propto R_\odot(t)^2$ to an accuracy of $\pm 0.5\%$. This transition from $L_\odot(t) \propto R_\odot(t)^{2.5}$ to $L_\odot(t) \propto R_\odot(t)^2$ can be seen clearly in Figure 2.

Table 3 gives the calculated effective temperature of the standard model, T_{eff}, as a function of solar age. The effective temperature varies by only $\pm 1.5\%$ over the entire period from the zero-age main sequence to an age of 8×10^9 yr and only by $\pm 0.7\%$ from 2×10^9 to 8×10^9 yr.

The relation between $L_\odot(t)$ and $R_\odot(t)$ discussed above can be restated using the calculated time dependence of the solar effective temperature, which is summarized in Table 3. In the period between 4 and 8 Gyr, the effective temperature is essentially constant (to an accuracy of $\pm 0.25\%$). This constancy of the effective temperature results in the scaling relation $L_\odot(t) \propto R_\odot(t)^2$ that is valid in this period. The effective temperature changes by an order of magnitude larger fraction during the evolution up to the present-age Sun, which results in a dependence closer to $L_\odot \propto R_\odot^{2.5}$ (see also Fig. 2 of Demarque & Guenther 1991).

3.2. *Energy Fractions*

Figure 3 shows, for the standard model, the energy generated by different nuclear fusion reactions as a function of solar age. The present-day total solar luminosity, $L_\odot(\text{today})$, is the unit of luminosity in Figure 3.

The branch of the *p-p* chain that is denoted in Figure 3 by *p-p* + ^{3}He-^{3}He (*dashed curve*) proceeds primarily through the reactions $p(p, e^+\nu_e)^2\text{H}(p, \gamma)^3\text{He}(^3\text{He}, 2p)^4\text{He}$. For simplicity, we include all *p-p* reactions in this sum but do not show explicitly the *pep*-reactions in the above scheme. The small energy contribution due to *pep*-reactions is included in the calculations that led to Figure 3. The ^{3}He-^{4}He branch (*dot-dashed curve*) includes the nuclear reactions that produce both the ^{7}Be and the ^{8}B neutrinos: $^3\text{He}(^4\text{He}, \gamma)^7\text{Be}(e^-, \nu_e)^7\text{Li}(p, {}^4\text{He})^4\text{He}$ and $^3\text{He}(^4\text{He}, \gamma)^7\text{Be}(p, \gamma)^8\text{B}(^4\text{He} + e^+ + \nu_e)^4\text{He}$. The CNO reactions are denoted by CNO in Figure 3.

The branch that terminates via the ^{3}He-^{3}He reaction dominates the solar energy generation throughout the main-sequence lifetime shown in Figure 3, although the CNO reactions overtake the ^{3}He-^{4}He branches at an age of about 8×10^9 yr. At an age of 1×10^9 yr, 96.7% of the solar luminosity is generated through *p-p* reactions plus the ^{3}He-^{3}He termination, 2.8% through the ^{3}He-^{4}He termination, and only 0.5% through the CNO cycle. The situation gradually changes as the Sun heats up. At the present epoch, the ^{3}He-^{3}He termination produces 87.8% of the solar luminosity and the branches terminating through the

TABLE 3

CALCULATED EFFECTIVE TEMPERATURE AS A FUNCTION OF SOLAR AGE FOR THE STANDARD MODEL

Age	T_{eff}	Age	T_{eff}
0.0.....	0.973	4.5.....	1.000
0.5.....	0.983	5.0.....	1.001
1.0.....	0.985	5.5.....	1.002
1.5.....	0.987	6.0.....	1.003
2.0.....	0.990	6.5.....	1.003
2.5.....	0.992	7.0.....	1.003
3.0.....	0.994	7.5.....	1.001
3.5.....	0.996	8.0.....	1.000
4.0.....	0.998	...	...

NOTE.—The solar age is measured in units of 10^9 yr, and the solar effective temperature is measured in units of the present-epoch effective temperature.

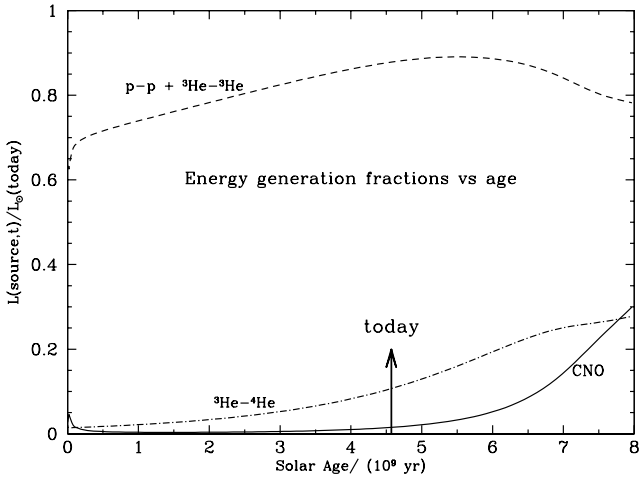

FIG. 3.—Fraction in the standard model of the solar luminosity produced by different nuclear fusion reactions vs. solar age. The luminosity generated by the *p-p* nuclear fusion branch that is terminated by the ^{3}He-^{3}He reaction is marked by a dashed curve in the figure, and the luminosity produced by the *p-p* branches that proceed through the ^{3}He-^{4}He reaction is denoted by a dot-dashed curve. The luminosity generation by the CNO cycle is indicated by a solid line. The unit of luminosity is the present-day total solar luminosity. At the present epoch, the *p-p* + ^{3}He-^{3}He reactions produce 87.8% of the solar luminosity and the branches terminating through the ^{3}He-^{4}He reaction generate 10.7% of the solar luminosity. The CNO cycle produces 1.5% of the present-epoch luminosity. [*See the electronic edition of the Journal for a color version of this figure.*]

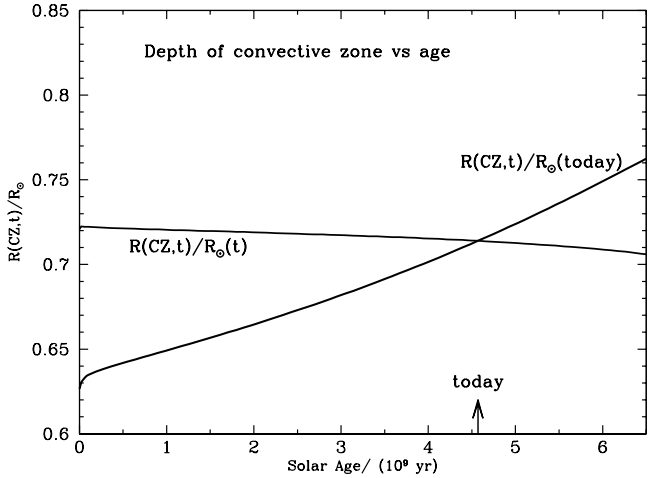

FIG. 4.—Depth of the convective zone, R(CZ, t), as a function of age for the standard solar model. The depth of the convective zone is approximately proportional to the contemporary solar radius. The solar age is measured in units of 10^9 yr. [*See the electronic edition of the Journal for a color version of this figure.*]

^{3}He-^{4}He reaction generate 10.7% of the solar luminosity. The CNO cycle produces 1.5% of the present-epoch luminosity. By the time the standard solar model reaches an age of 8×10^9 yr, the percentages are 57.6%, 20.4%, and 22.0%, respectively, for ^{3}He-^{3}He, ^{3}He-^{4}He, and CNO reactions. The energy loss due to gravitational energy expansion ranges from -0.03% to -0.04% to -0.07% as the Sun's age increases from 1×10^9 yr to the present epoch to 8×10^9 yr.

3.3. *Convective Zone*

Figure 4 shows the depth of the convective zone, R(CZ, t), as a function of age for the standard solar model. Correspondingly, Figure 5 shows the mass of the convective zone, M(CZ, t), as a function of age. In both cases, the temporal dependence from the zero-age main sequence to the current epoch is describable by a simple function of $R_\odot(t)/R_\odot$(today).

We limit the time period covered in Figures 4 and 5 to be less than 6.5×10^9 yr, since between 6.5×10^9 and 7.0×10^9 yr of age semiconvection begins to influence the computed R(CZ, t) and M(CZ, t). The evolution of the depth of the solar convective zone was previously studied by Demarque & Guenther (1991) in an investigation that did not include element diffusion.

The occurrence of semiconvection in evolved solar models is discussed here for the first time, to the best of our knowledge. The onset of semiconvection is triggered by the effects of element diffusion, which was first included in detailed solar models in the early 1990s (see, e.g., Bahcall & Loeb 1990; Proffitt & Michaud 1991; Bahcall & Pinsonneault 1992).

The process works essentially as follows. The timescale for diffusion decreases as the surface convective zone becomes shallower; the metal abundance increases steadily below the surface convective zone. At some point in the evolutionary history, near an age of 6.5×10^9 yr, the opacity from the enhanced metal abundance below the surface convective zone becomes large enough to make the metal-rich radiative layers below the surface convective zone convectively unstable. However, the mixing of the metals into the envelope causes a local drop in the metal abundance Z and the opacity κ at the base of the convective zone. This result in turn causes the convective zone to recede until the metal abundance builds up again. Richer, Michaud, & Turcotte (2000) discuss a related phenomenon in A and F stars.

We noticed the existence of semiconvection in our standard solar model only because we made precise plots of the depth and mass of the convective zone as a function of time (see Figs. 4 and 5). The effects of semiconvection were not noticeable in plots of external quantities such as the solar luminosity or effective temperature (see § 3.1). In our current code, if a region is convectively unstable according to the

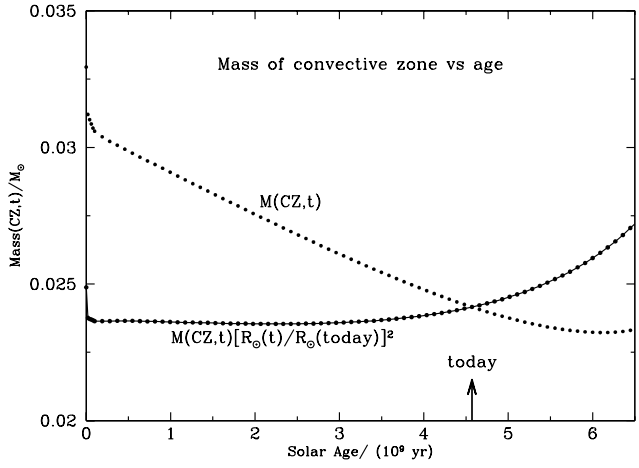

FIG. 5.—Mass included within the convective zone, M(CZ, t), as a function of age for the standard solar model. The mass of the convective zone is measured in units of $M_\odot$(today), and the solar age is measured in units of 10^9 yr. The mass of the convective zone is approximately proportional to $R_\odot(t)^{-2}$. [*See the electronic edition of the Journal for a color version of this figure.*]

Schwarzschild criterion, then we instantly mix this material with the other material in the convective zone. A more accurate treatment, which allows for the possibility of a composition gradient being established at the base of the convective zone, is required to calculate reliably the influence of semiconvection once it begins to be perceptible in the numerical solutions (see, e.g., Merryfield 1995; Canuto 2000 and references therein). This is why we have terminated the plots of $R(\mathrm{CZ}, t)$ and $M(\mathrm{CZ}, t)$ at a solar age of 6.5×10^9 yr.

From the zero-age main sequence to the present solar age, the depth of the convective zone is approximately proportional to the contemporary solar radius, $R_\odot(t)$, i.e.,

$$0.714 \leq \frac{R(\mathrm{CZ}, t)}{R_\odot(t)} \leq 0.722 \, . \tag{2}$$

The zero-age main-sequence value is $R(\mathrm{CZ}, t = 0) = 0.627\ R_\odot(\mathrm{today})$, and the present-day value is $R(\mathrm{CZ}, \mathrm{today}) = 0.714\ R_\odot(\mathrm{today})$, which corresponds to an approximately 14% decrease in the depth of the convective zone over the age of the Sun. However, if we normalize the depth of the convective zone to the contemporary solar radius, the change is very small, $R(\mathrm{CZ}, t = 0) = 0.722\ R_\odot(t = 0)$ and $R(\mathrm{CZ}, \mathrm{today}) = 0.714\ R_\odot(\mathrm{today})$. After 6.5×10^9 yr, $R(\mathrm{CZ}, t = 6.5) = 0.764\ R_\odot(\mathrm{today})$and, in terms of the contemporary solar radius, $R(\mathrm{CZ}, t = 6.5) = 0.706\ R_\odot(t = 6.5)$. The relative evolution between the convective zone depth and the total solar radius, $d[R(\mathrm{CZ}, t)/R_\odot(t)]/dt = -0.002$ per 10^9 yr, is very slow.

Over the period from the initial-age main sequence to the present epoch, the mass of the solar convective zone decreases with time as $R_\odot(t)^{-2}$,

$$M(\mathrm{CZ}, t) R_\odot(t)^2 = \mathrm{constant} \, , \tag{3}$$

to an accuracy of about $\pm 1\%$. The zero-age main-sequence value of the mass included within the convective zone is $0.0329\ M_\odot$, which decreases to $0.02415\ M_\odot$ at the present epoch. However, this proportionality is no longer valid for larger ages, as can be seen in Figure 5. The mass of the convective zone is $M(\mathrm{CZ}, 6.5) = 0.0233\ M_\odot$ at 6.5×10^9 yr. At about 6.8×10^9 yr, the previous monotonic decrease of the mass of the convective zone is reversed and $M(\mathrm{CZ}, t)$ begins to increase with time. This behavior is not shown in Figure 5 since the calculated increase in the mass of the convective zone occurs in the same time frame as the onset of semiconvection.

Figure 6 shows some properties at the base of the convective zone as a function of solar age. The figure displays the time dependence of the temperature, $T(\mathrm{CZ}, t)$ (*solid curve*); the density, $\rho(\mathrm{CZ}, t)$ (*dotted curve*); the pressure, $P(\mathrm{CZ}, t)$ (*short-dashed curve*); and the radiative opacity, $\kappa(\mathrm{CZ}, t)$ (*long-dashed curve*). For convenience in plotting, each of the physical variables has been divided by its value at the current epoch. In cgs units, the standard model parameters have the following values at an age of 4.57×10^9 yr: $T(\mathrm{CZ}, \mathrm{today}) = 2.18 \times 10^6$ K, $\rho(\mathrm{CZ}, \mathrm{today}) = 0.19$, $P(\mathrm{CZ}, \mathrm{today}) = 5.58 \times 10^{13}$, and $\kappa(\mathrm{CZ}, \mathrm{today}) = 20.5$.

The temperature at the base of the convective zone decreases by 14% from the zero-age main sequence to the current solar age, i.e., to a good approximation

$$T(\mathrm{CZ}, t) \propto R(\mathrm{CZ}, t)^{-1} \, . \tag{4}$$

The opacity at the base of the convective zone decreases by 6% over the same period. The density and the pressure at the base of the convective zone decrease by much larger quantities, by factors of 2.1 and 2.3, respectively. Equation (4) is valid to an accuracy of about $\pm 1\%$ throughout the 6.5×10^9 yr shown in Figure 6.

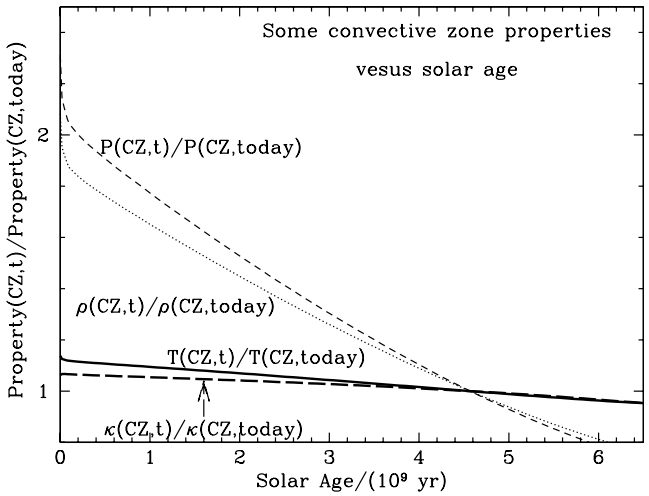

FIG. 6.—Some properties at the base of the convective zone as a function of age for the standard solar model. The properties shown are the temperature, $T(\mathrm{CZ}, t)$ (*solid curve*); the density, $\rho(\mathrm{CZ}, t)$ (*dotted curve*); the pressure, $P(\mathrm{CZ}, t)$ (*short-dashed curve*); and the radiative opacity, $\kappa(\mathrm{CZ}, t)$ (*long-dashed curve*). All of the quantities are normalized by dividing by their values at the present epoch. After 6.5×10^9 yr, semiconvection begins to be important. [*See the electronic edition of the Journal for a color version of this figure.*]

The base of the convective zone is defined by the Schwarzschild criterion. Because the adiabatic gradient is nearly constant in time, the equations of stellar structure imply that the quantity $\kappa PL/MT^4$ will be approximately constant at the base of the convective zone. From Figure 6, we see that both the opacity and the temperature decrease slowly at the base of the convective zone. Solar models therefore compensate for the increase of the luminosity by the decrease of the pressure at the boundary between radiative and convective equilibrium.

3.4. *Central Values of Temperature, Density, and Pressure*

Figure 7 shows the time dependence of the central values for the temperature, density, and pressure of the standard solar model. The results are normalized to the computed values for the present epoch.

Over the 8×10^9 yr shown in Figure 7, the central temperature increases by about 39%. The central temperature is 13.5×10^9 K at the zero-age main sequence and 15.7×10^9 K at the current epoch; the central temperature of the model reaches 18.8×10^9 K at a solar age of 8×10^9 yr. This increase is very similar to that of the solar radius. In fact, the central value of the temperature is, to a reasonable approximation, proportional to the solar radius, $R_\odot(t)$. The ratio

$$\frac{T_c(t)}{R_\odot(t)} = \mathrm{constant} \tag{5}$$

to an accuracy of $\pm 1.5\%$ ($\pm 3\%$) from the zero-age main sequence to the current epoch (to a solar age of 6.5×10^9 yr).

The Sun derives its luminosity by burning hydrogen into helium. The hydrogen mass fraction at the center of the Sun, X_c, decreases from 0.708 at the zero-age main sequence to 0.340 at the current epoch, a decrease by more than a factor

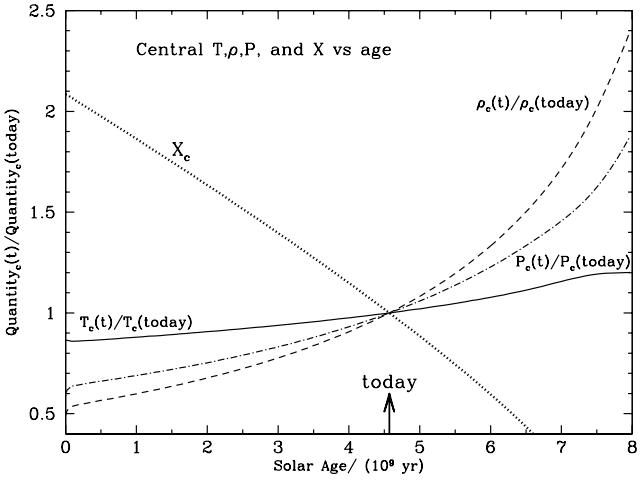

FIG. 7.—Temporal evolution of the central temperature, density, pressure, and hydrogen mass fraction. The figure shows the computed values for the standard solar model of the central temperature (*solid line*), pressure (*dot-dashed line*), density (*dashed line*), and hydrogen mass fraction (*dotted line*). [*See the electronic edition of the Journal for a color version of this figure.*]

of 2. At an age of 6.5×10^9 yr, the mass fraction has decreased to 0.145, a decrease by a factor of almost 5 from the zero-age value. The remaining hydrogen is burned very quickly, with X_c reaching 0.008 at a solar age of 8×10^9 yr.

3.5. *Large and Small p-Mode Separations*

The *p*-mode oscillation frequencies change as the structure of the Sun evolves with age. Since only low-degree modes (small spherical harmonic, l) are observable for stars other than the Sun, we shall discuss the changes in just these modes.

For the high-order (large radial node, n), low-degree modes that are expected to be observed in stars, the frequencies satisfy the following relation to a good approximation (e.g., Tassoul 1980):

$$\nu_{nl} \simeq \Delta\left(n + \frac{l}{2} + \alpha\right). \tag{6}$$

Here ν_{nl} is the cyclic frequency of a mode of order n and degree l, and α is in general a slowly varying function of frequency. The departures from the simple relation in equations (6) and (9) provide diagnostic information about the stellar interior.

In the simplest approximation, the modes are uniformly spaced in radial order. The so-called large separation, Δ, is approximately constant,

$$\Delta(n, l) \simeq \nu_{n,l} - \nu_{n-1,l}\,. \tag{7}$$

The large separation Δ can be related to the sound speed by the formula

$$\Delta = \left[2\int_0^R \frac{dr}{c(r)}\right]^{-1}. \tag{8}$$

In equation (8), the integration variable is the distance r from the center of the star; the range of integration is from the solar center to the surface radius R. The sound speed is denoted by c. According to this equation, Δ is the inverse of the sound travel time across a stellar diameter. Thus, as the sound speed decreases with increasing solar age, the sound travel time increases and the large separations decrease. It also follows from equation (6) that the frequencies of modes whose degrees have the same parity approximately coincide,

$$\nu_{nl} \simeq \nu_{n-1,l+2}\,. \tag{9}$$

The departure from equation (9), the "small frequency separation," is defined by the relation

$$d_{nl} = \nu_{nl} - \nu_{n-1,l+2} \tag{10}$$

and is sensitive to conditions in the stellar core. The small separation d_{nl} depends on the gradient of the solar sound speed, particularly near the stellar core. The average over n of d_{nl} is proportional to a quantity D given by

$$D \simeq -\frac{1}{4\pi^2 x_0}\int_0^R \frac{dc}{dr}\frac{dr}{r}, \tag{11}$$

where x_0 is a suitable reference value of $n + l/2$ (Scherrer et al. 1983; Christensen-Dalsgaard 1988). The average small frequency separations provide a measure of the age of the star (see, e.g., Ulrich 1986; Christensen-Dalsgaard 1988; Guenther 1991). The solar sound speed decreases with age. The main decrease occurs near the core, in large part because of an increase with age of the mean molecular weight as a result of hydrogen being converted to helium. The sound speed develops a local minimum at the center. Thus, dc/dr is positive near the center of the star (in contrast to the negative gradient elsewhere), which reduces the value of the integral in equation (11). The small frequency separations are more sensitive to age than the large frequency separations, although the large separations also decrease with increasing age.

Table 4 lists for our standard solar model the calculated unweighted averages (denoted by angular brackets) of the large and small frequency separations as a function of solar age. The large separations were averaged over modes with

TABLE 4

AVERAGE LARGE AND SMALL FREQUENCY SEPARATIONS OF LOW-DEGREE MODES OF A SOLAR MODEL AS A FUNCTION OF SOLAR AGE

Parameters	$\langle\Delta(n, l)\rangle$	$\langle d_{n0}\rangle$	$\langle d_{n1}\rangle$
Age (Gyr):			
0.000	170.57	19.65	31.34
0.547	164.03	17.84	28.76
1.083	160.22	16.47	27.55
1.888	154.87	15.25	25.08
2.246	152.62	14.70	24.29
2.871	147.98	13.42	22.29
3.408	144.52	12.60	21.10
4.034	140.16	11.67	19.68
4.570	136.10	10.57	17.97
5.017	132.87	9.92	16.95
5.464	129.57	8.98	15.53
5.911	126.19	8.37	14.50
6.358	122.82	7.45	13.09
6.805	119.27	6.90	12.07
7.252	115.75	6.02	10.65
Observations:			
BiSON + LOWL	135.33	10.51	17.81
GOLF	135.12	10.46	17.75
GOLF2	134.84	10.22	17.18
GONG	134.86	10.04	18.24
MDI	134.95	10.14	17.64

NOTE.—Also listed are the observed values for the Sun. All splittings are given in units of μHz.

$l = 0$, 1, 2, and 3 and n between 10 and 22. This range of n was chosen because it is the observed range for most data sets. The set of small separations given in the third column of Table 4 (d_{n0}) was calculated for $l = 0$ and $l = 2$ modes; the small separations in the fourth column of Table 4 (d_{n1}) were calculated for $l = 1$ and $l = 3$ modes. The small separations were averaged over the same range of n as the large separations.

As expected, both large and small separations decrease with time, with small separations decreasing much more rapidly than large separations. The decrease is slightly larger for the $l = 0$, 2 separations than for the $l = 1$, 3 separations because the $l = 0$ modes are more sensitive to core conditions than the $l = 1$ modes.

Table 4 also shows the results obtained from different helioseismology observations. References for the observations are given in § 6, which is where we discuss sound speeds. We do not include in Table 4 results for the large and small separations for LOWL1 because for this data set there are not enough low-degree modes to form a robust average over the range of selected n.

The calculated values for a solar age of 4.57 Gyr should be compared with the observed values listed in Table 4. The calculated large separation is slightly different from the observed values, which may reflect an uncertainty in the detailed physics of the surface layers. The uncertainty in the physics of the surface layers introduces errors in the calculated model frequencies. These frequency-dependent errors are not completely removed in the process of calculating the large separations from the standard solar model. The surface uncertainties are removed more successfully in the calculation of the small separations.

4. VARIANT AND DEVIANT SOLAR MODELS

In this section we describe 11 solar models, seven of which are slight variants on the theme of the standard solar model (see § 4.1) and four of which are deficient in one or more significant aspects of the physics used in their construction (see § 4.2). Nine of these solar models have been described in detail in BPB00, where their helioseismological properties were investigated extensively. Hence, the descriptions here will be brief.

Since the first report (Davis, Harmer, & Hoffman 1968) that the solar neutrino event rate in the chlorine experiment was less than the predicted rate (Bahcall, Bahcall, & Shaviv 1968), obtained by using the then standard solar model and the then standard electroweak theory, there have been many studies of deviant solar models that were designed to "explain" the solar neutrino problem. The first nonstandard solar model was proposed by Ezer & Cameron (1968), who suggested that the flux of ^{8}B neutrinos could be reduced if the central hydrogen abundance could be maintained near its initial value by continuous mixing in the solar core. (For a discussion of, and references to, the extensive early work on this problem, see Bahcall 1989.) With the advent of precise measurements of solar p-modes that extend deep into the solar interior, many nonstandard models have been explicitly shown to be inconsistent with the inferred solar sound speeds (Bahcall et al. 1997) or the p-mode frequencies (Guenther & Demarque 1997).

We explore here the range of solar parameters predicted by various nonstandard models, even those that are strongly inconsistent with helioseismological data. Our purpose is to set extreme limits on predicted solar parameters, such as the luminosity evolution or neutrino emission, rather than the traditional goal of avoiding new neutrino physics. Other authors have used nonstandard solar models in connection with helioseismology for a variety of different applications, including, for example, constraining the cross section for the p-p interaction (Antia & Chitre 1999), limiting the amount of mass loss from the Sun (Guzik & Cox 1995), and constraining the amount of anomalous energy transport by WIMPS (Christensen-Dalsgaard 1992). Turcotte & Christensen-Dalsgaard (1998) have considered the impact of changes in heavy-element abundances on the properties of some models; the pattern of effects they found is consistent with that obtained here.

Tables 5 and 6 summarize some of the important physical characteristics of the complete set of the nine solar models whose helioseismological properties we studied in BPB00 plus two models with slightly lower values of Z/X that are studied here for the first time. We present in Table 5 for each of the models the central temperature, density, and pressure; the helium and heavy-element mass fractions in the initial model; and the helium and heavy-element mass fractions in the solar center. We give in Table 6 the helium and heavy-element abundances at the solar surface; the mixing length parameter, α; and the radius and temperature

TABLE 5

SOME INTERIOR CHARACTERISTICS OF THE SOLAR MODELS

Model	T_c	ρ_c	P_c	$Y_{\rm init}$	$Z_{\rm init}$	Y_c	Z_c
Standard	15.696	152.7	2.342	0.2735	0.0188	0.6405	0.0198
NACRE	15.665	151.9	2.325	0.2739	0.0188	0.6341	0.0197
AS00	15.619	152.2	2.340	0.2679	0.0187	0.6341	0.0197
GN93	15.729	152.9	2.342	0.2748	0.02004	0.6425	0.02110
Pre-M.S.	15.725	152.7	2.339	0.2752	0.02003	0.6420	0.02109
Rotation	15.652	148.1	2.313	0.2723	0.01934	0.6199	0.02032
Radius$_{78}$	15.729	152.9	2.342	0.2748	0.02004	0.6425	0.02110
Radius$_{508}$	15.728	152.9	2.341	0.2748	0.02004	0.6425	0.02110
No Diffusion	15.448	148.6	2.304	0.2656	0.01757	0.6172	0.01757
Old Physics	15.787	154.8	2.378	0.2779	0.01996	0.6439	0.02102
$S_{34} = 0$	15.621	153.5	2.417	0.2722	0.02012	0.6097	0.02116
Mixed	15.189	90.68	1.728	0.2898	0.02012	0.3687	0.02047

NOTE.—The quantities T_c (in units of 10^7 K), ρ_c (10^2 g cm^{-3}), and P_c (10^{17} ergs cm^{-3}) are the present-epoch central temperature, density, and pressure; Y and Z are the helium and heavy-element mass fractions, where the subscript "init" denotes the zero-age main-sequence model and the subscript "c" denotes the center of the solar model.

TABLE 6

SOME CHARACTERISTICS OF THE CONVECTIVE ZONES OF SOLAR MODELS AT THE CURRENT EPOCH

Model	Y_s	Z_s	α	R(CZ) ($R_\odot$)	M(CZ) ($M_\odot$)	T(CZ) (10^6 K)
Standard	0.2437	0.01694	2.04	0.7140	0.02415	2.18
NACRE	0.2443	0.01696	2.04	0.7133	0.02451	2.19
AS00	0.2386	0.01684	2.05	0.7141	0.02394	2.18
GN93	0.2450	0.01805	2.06	0.7124	0.02457	2.20
Pre-M.S.	0.2455	0.01805	2.05	0.7127	0.02443	2.20
Rotation	0.2483	0.01797	2.03	0.7144	0.02388	2.15
Radius_{78}	0.2450	0.01806	2.06	0.7123	0.02461	2.20
Radius_{508}	0.2450	0.01806	2.06	0.7122	0.02467	2.20
No Diffusion	0.2655	0.01757	1.90	0.7261	0.02037	2.09
Old Physics	0.2476	0.01796	2.04	0.7115	0.02455	2.21
$S_{34} = 0$	0.2422	0.01811	2.03	0.7151	0.02309	2.17
Mixed	0.2535	0.01782	1.85	0.7315	0.01757	2.02

NOTE.—Here Y_s and Z_s are the surface helium and heavy-element abundances, α is the mixing length parameter, R(CZ) and T(CZ) are the radius and temperature at the base of the convective zone, and M(CZ) is the mass included within the convective zone.

at the base of the convective zone, as well as the mass included in the convective zone. All quantities are shown for the model at the present epoch.

We will now define the 11 variant and deviant solar models.

4.1. *Variant Solar Models*

The NACRE model was constructed using the same input physics as our standard model except that we use for the NACRE model the charged particle fusion cross sections recommended in the NACRE compilation (Angulo et al. 1999). We specify the fusion cross sections used for this model more fully in § 5.1.3. The model GN93 was considered our standard model in BPB00 and differs only in the adopted value of $Z/X = 0.0245$ (Grevesse & Noels 1993) from the current standard model (see § 2), which has $Z/X = 0.0230$ (Grevesse & Sauval 1998). The model AS00 is the same as the two models described above except that it has lower heavy-element abundance $Z/X = 0.0226$ (Asplund 2000). As a consequence of a more detailed calculation of the solar atmosphere, Asplund (2000) suggests that all meteoritic abundances should be adjusted downward by 0.04 dex. All of the models described below, in § 4.2 as well as in this subsection, use the Grevesse & Noels (1993) composition mix with $Z/X = 0.0245$.

Model Pre-M.S. is evolved from the pre–main-sequence stage but otherwise is the same as our standard model. The model Rotation incorporates mixing induced by rotation and is a reasonable upper bound to the degree of rotational mixing that is consistent with the observed depletion of lithium in the Sun (Pinsonneault et al. 1999).[5] The prescriptions for calculating this model are described in § 5 of Pinsonneault (1997) and in BPB00. There has been considerable discussion recently regarding the precise value of the solar radius (see Antia 1998; Schou et al. 1997; Brown & Christensen-Dalsgaard 1998) and some discussion of the effects of the uncertainty in radius on the quantities inferred from the helioseismological inversions (see Basu 1998). We have therefore considered two models that were constructed with the same input physics as BP2000 but have model radii that differ from the radius assumed in constructing the standard model. Radius_{78} has a radius of 695.78 Mm, which is the radius that has been determined from the frequencies of f-modes (see Antia 1998), and Radius_{508} has a radius of 695.508 Mm, which is the solar radius as determined by Brown & Christensen-Dalsgaard (1998), who used the measured duration of solar meridian transits during 1981–1987 and combined these measurements with models of the solar limb-darkening function to estimate the value of the solar radius.

All of these variant models are approximately as consistent with the helioseismological evidence as the standard model (see BPB00). For example, the rms sound speed differences between the variant models and BP2000 are 0.03% (Pre-M.S.), 0.08% (Rotation), 0.15% (Radius_{78}), and 0.03% (Radius_{508}). The average difference (rms) between the four variant models and the standard model is 0.07%. We shall see in § 5 that the differences predicted by these models for the important neutrino fluxes are all less than 5%.

4.2. *Deviant Solar Models*

The model "Old Physics" was constructed using the old Yale equation of state (see Guenther et al. 1992), supplemented with the Debye-Hückel correction (see Bahcall et al. 1968) and older OPAL radiative opacities (Iglesias, Rogers, & Wilson 1992; Kurucz 1991). The model includes helium and heavy-element diffusion and nuclear reaction cross section data in the same way as our standard model. The $S_{34} = 0$ model was calculated assuming that the rate of the $^3\text{He}(\alpha, \gamma)^7\text{Be}$ reaction is zero, which implies that no ^{7}Be or ^{8}B neutrinos are produced. In the standard solar model, about 12% of the terminations of the *p-p* chain involve the $^3\text{He}(\alpha, \gamma)^7\text{Be}$ reaction, whose rate is proportional to S_{34}. The No Diffusion model does not include helium or heavy-element diffusion and therefore represents the state of the art in solar modeling prior to 1992 (see Bahcall & Ulrich 1988; Bahcall & Pinsonneault 1992; Proffitt 1994). The

[5] The Rotation model discussed here differs somewhat from the rotation model analyzed in BPB00 in that the metals heavier than CNO were inadvertently not mixed in the previous version of this model. The rotation profile computed from this model does not match precisely the best current estimates of the rotation profile in the inner regions of the Sun. The case considered here corresponds to the maximum amount of mixing. Richard et al. (1996) consider solid body rotation, which corresponds to what is likely to be the minimum amount of mixing. Both of these models yield similar results for the effect of rotation on diffusion, which is the principal way that rotation affects solar neutrino fluxes.

model Mixed has an artificially mixed core, with the inner 50% by mass (25% by radius) required to be chemically homogeneous at all times. This model was constructed to be similar to the prescription of Cumming & Haxton (1996), who changed by hand the ^{3}He abundance as a function of radius in the final BP95 (Bahcall & Pinsonneault 1995) solar model in order to minimize the discrepancy between measurements of the total event rates in neutrino experiments and the calculated event rates. Cumming & Haxton (1996) did not calculate the time evolution of their model.

We showed in BPB00 that the Mixed, No Diffusion, and $S_{34} = 0$ models are strongly disfavored by helioseismological data. We use these deviant (or deficient) models here to test the robustness of the discrepancies between solar model predictions and solar neutrino measurements. (For references and discussions to earlier work on these deviant models, see Bahcall 1989; Christensen-Dalsgaard 1995; Bahcall et al. 1997; Guenther & Demarque 1997; Cox, Kidman, & Newman 1985). We have already seen in Figure 2 that the luminosity evolution predicted by solar models is essentially the same for the deviant models and for the standard solar model.

5. NEUTRINO PHYSICS

This section presents neutrino fluxes and predicted event rates in different solar neutrino experiments; the fluxes and event rates are calculated using the 11 solar models described in § 4. We also give other aspects of the solar model that influence the interpretation of solar neutrino experiments.

As described in § 2.2, we present on-line (see footnote 4 for the URL) a detailed numerical table that gives the fraction of each of the eight important neutrino fluxes that is produced in each spherical shell. These neutrino production fractions are important for calculating the effect of MSW (matter) oscillations in the Sun but will not be discussed further here.

Section 5.1 presents the fluxes of electron-type neutrinos that are produced in the Sun according to the standard solar model and to the eight variant solar models considered in this paper. We compare the results of these predictions with measurements of the total rates in the chlorine solar neutrino experiment, the SAGE and GALLEX+GNO gallium experiments, and the Kamiokande and Super-Kamiokande water Cerenkov detectors. We also describe in this section how we estimate the errors (asymmetric in some cases) on the predicted fluxes and event rates.

In § 5.2 we present detailed results for the electron number density versus solar radius. The MSW conversion of electron-type neutrinos to other neutrino types depends upon the radial distribution of the electron number density. In previous presentations of the standard model, we have not given the electron number density in the outer parts of the Sun with sufficient precision to permit calculations of a subset of the currently allowed matter transitions. Section 5.4 presents the calculated time dependences of the most important solar neutrino fluxes, the *pp*, ^{7}Be, ^{8}B, and ^{13}N neutrino fluxes.

5.1. *Neutrino Fluxes and Experimental Event Rates at the Current Epoch*

We present in § 5.1.1 the neutrino fluxes and experimental event rates predicted by the standard model and contrast these results with the observed rates. In § 5.1.2 we describe the procedures and the ingredients used to calculate the uncertainties in the neutrino fluxes and the event rates. We compare in § 5.1.4 the calculated neutrino fluxes and experimental event rates for the eight variant and deviant solar models with the results for the standard model and with the measured solar neutrino event rates.

5.1.1. *Standard Model*

Table 7 gives the neutrino fluxes and their uncertainties for our standard solar model. In order to obtain the most precise values that we can for the predicted fluxes, we have recomputed the standard model discussed elsewhere in this paper. We use in this subsection the most recently determined absolute value for the solar luminosity, 3.842×10^{33} ergs^{-1} (Fröhlich & Lean 1998; Crommelynck et al. 1996), which is 0.2% smaller than the value used in the model calculations discussed elsewhere in this paper. The largest changes due to the 0.2% decrease in the solar luminosity are a 2% decrease in the ^{8}B neutrino flux and a 1% decrease in the ^{7}Be neutrino flux. All other quantities calculated in this paper are changed by negligible amounts.

The adopted uncertainties in different input parameters are given in Table 2 of BBP98. We also present in Table 7 the calculated event rates in the chlorine, gallium, and lithium experiments. The rate in the Super-Kamiokande experiment is usually quoted as a fraction of the best estimate theoretical flux of ^{8}B neutrinos, assuming an undistorted (standard) energy spectrum.

Table 8 compares the predictions of the combined standard model, i.e., the standard solar model (BP2000) and the standard electroweak theory (no neutrino oscillations), with the results of the chlorine, GALLEX+GNO, SAGE, Kamiokande, and Super-Kamiokande solar neutrino experiments. The observed rate in the chlorine experiment is 2.56 ± 0.23 SNU (Lande 2001; Davis 1994; Cleveland et al. 1998), which is to be compared to the calculated value of $7.6^{+1.3}_{-1.1}$ SNU. This discrepancy between calculated and observed neutrino capture rates has been approximately the same for more than three decades (see Bahcall et al. 1968; Davis et al. 1968; Bahcall 1989).

TABLE 7

STANDARD MODEL PREDICTIONS (BP2000)

Source	Flux (10^{10} cm^{-2} s^{-1})	Cl (SNU)	Ga (SNU)	Li (SNU)
pp	$5.95(1.00^{+0.01}_{-0.01})$	0.0	69.7	0.0
pep	$1.40 \times 10^{-2}(1.00^{+0.015}_{-0.015})$	0.22	2.8	9.2
hep	9.3×10^{-7}	0.04	0.1	0.1
^{7}Be	$4.77 \times 10^{-1}(1.00^{+0.10}_{-0.10})$	1.15	34.2	9.1
^{8}B	$5.05 \times 10^{-4}(1.00^{+0.20}_{-0.16})$	5.76	12.1	19.7
^{13}N	$5.48 \times 10^{-2}(1.00^{+0.21}_{-0.17})$	0.09	3.4	2.3
^{15}O	$4.80 \times 10^{-2}(1.00^{+0.25}_{-0.19})$	0.33	5.5	11.8
^{17}F	$5.63 \times 10^{-4}(1.00^{+0.25}_{-0.25})$	0.0	0.1	0.1
Total	...	$7.6^{+1.3}_{-1.1}$	128^{+9}_{-7}	$52.3^{+6.5}_{-6.0}$

NOTE.—Solar neutrino fluxes and neutrino capture rates, with 1 σ uncertainties from all sources (combined quadratically). The tabulated fluxes correspond to a present-day solar luminosity of 3.842×10^{33} ergs^{-1}. The observed capture rates are 2.56 ± 0.23 SNU (chlorine; Lande 2001) and 74.7 ± 5.0 SNU (combined SAGE and GALLEX+GNO; Hampel et al. 1999; Abdurashitov et al. 1999; Bellotti et al. 2001). The ^{8}B flux measured by the Super-Kamiokande experiment is $2.40 \pm 0.03(\text{stat})^{+0.08}_{-0.07}(\text{syst.})$ cm^{-2} s^{-1} (Suzuki 2001). The cross sections for neutrino absorption on chlorine are from Bahcall et al. 1996, the cross sections for gallium are from Bahcall 1997, and the cross sections for ^{7}Li are from Bahcall 1989, 1994.

TABLE 8

SOLAR NEUTRINO RATES

Experiment	BP2000	Measured	Measured/BP2000
Chlorine	$7.6^{+1.3}_{-1.1}$	2.56 ± 0.23	0.34 ± 0.06
GALLEX+GNO	128^{+9}_{-7}	$74.1^{+6.7}_{-7.8}$	0.58 ± 0.07
SAGE.....	128^{+9}_{-7}	$75.4^{+7.8}_{-7.4}$	0.59 ± 0.07
^{8}B-Kamiokande	$5.05[1.00^{+0.20}_{-0.16}]$	$2.80[1.00 \pm 0.14]$	0.55 ± 0.13
^{8}B-Super-Kamiokande	$5.05[1.00^{+0.20}_{-0.16}]$	$2.40[1.00^{+0.04}_{-0.03}]$	0.48 ± 0.09
hep-Super-Kamiokande.....	9.3	$11.3(1 \pm 0.8)$	~ 1

NOTE.—Theory vs. experiment. The units are SNU (10^{-36} interactions atom^{-1} s^{-1}) for the radiochemical experiments: chlorine, GALLEX+GNO, and SAGE. The units for the ^{8}B and *hep* fluxes are, respectively, 10^6 and 10^3 cm^{-2} s^{-1}. The errors quoted for measured/BP2000 are the quadratically combined uncertainties for both BP2000 and the measured rates. For simplicity in presentation, asymmetric errors were averaged. References to the experimental results are given in the text and in Lande 2001, Bellotti et al. 2001, Gavrin 2001, Fukuda et al. 1996, and Suzuki 2001 for the chlorine, GALLEX+GNO, SAGE, Kamiokande, and Super-Kamiokande results.

The average of the SAGE (Abdurashitov et al. 1999; Gavrin 2001) and the GALLEX (Hampel et al. 1999) plus GNO (Bellotti et al. 2001) results is 74.7 ± 5.0 SNU, which is more than 6 σ away from the calculated standard rate of 128^{+9}_{-7} SNU.

After 1117 days of data acquisition, the flux of ^{8}B neutrinos measured by Super-Kamiokande is $[2.40 \pm 0.03(\text{stat})^{+0.08}_{-0.07}(\text{syst.})]10^{-6}$ cm^{-2} s^{-1} (Suzuki 2001; Fukuda et al. 1998), which corresponds to 0.475 of the BP2000 predicted flux.

Comparing the second and third columns of Table 8, we see that the predictions of the combined standard model differ by many standard deviations from the results of the solar neutrino experiments.

The flux of *hep* neutrinos was calculated for BP2000 using the most recent theoretical evaluation by Marcucci et al. (2000a, 2000b) of the cross section factor $S_0(hep)$, which is 4.4 times larger than the previous best estimate. The most recent preliminary report (after 1117 days of data) of the Super-Kamiokande collaboration (Suzuki 2001) is that the *hep* flux observed in their ν_e-e scattering experiment is 5.4 ± 4.5 times the best estimate from BBP98. Since the BP2000 estimate of the *hep* flux is a factor of 4.4 times larger than the flux quoted in BBP98, the best estimate theoretical *hep* flux now agrees with the best estimate experimental *hep* flux measurement, although we do not attach much significance to this agreement since we cannot quote an uncertainty on the theoretical estimate (see discussion of the *hep*-reaction in § 5.1.2).

The event rates predicted by BP2000 for the chlorine, gallium, and Super-Kamiokande solar neutrino experiments are within 2% of the rates predicted for the BBP98 standard solar models. As far as these experiments are concerned, the effect of using the improved heavy-element composition essentially cancels the effect of correcting the error in the opacity interpolation (see § 2.1). The difference in the ^{7}Be flux predicted by BBP98 and BP2000 is only 0.6%. The ^{7}Be flux will be measured by the BOREXINO solar neutrino experiment.

5.1.2. *Calculated Uncertainties*

We have calculated the uncertainties in the neutrino fluxes and in the experimental event rates by including the published errors in all experimental quantities and by taking account of the correlated influence of different input parameters using the results of detailed solar model calculations. The procedure for calculating the uncertainties has been developed over the past three decades and is described in detail in Bahcall (1989; see also Bahcall & Pinsonneault 1992, 1995; BBP98).

In order that the reader can see the specific implementation of the uncertainty calculations, we are making available the exportable FORTRAN code that evaluates the rates in different neutrino experiments and also calculates the uncertainties in the individual neutrino fluxes and experimental rates. The code, exportrates.f, is available on-line.[6]

The uncertainties in the nuclear fusion cross sections (except for *hep*; see below) were taken from Adelberger et al. (1998), the neutrino cross sections and their uncertainties are from Bahcall (1994, 1997) and Bahcall et al. (1996), the luminosity and age uncertainties were adopted from Bahcall & Pinsonneault (1995), the 1 σ fractional uncertainty in the diffusion rate was taken to be 15% (Thoul et al. 1994), and the opacity uncertainty was determined by comparing the results of fluxes computed using the older Los Alamos opacities with fluxes computed using the modern Livermore opacities (Bahcall & Pinsonneault 1992).

We follow the discussion in Bahcall & Pinsonneault (1995) and adopt a 1 σ uncertainty in the heavy-element abundance of

$$\sigma\left(\frac{Z}{X}\right) = \pm 0.061\left(\frac{Z}{X}\right). \quad (12)$$

This uncertainty spans the range of values recommended by Grevesse (1984), Grevesse & Noels (1993), and Grevesse & Sauval (1998) over the 14 yr period covered by the cited Grevesse et al. review articles. The uncertainty adopted here is about twice as large as the uncertainty recommended by Basu & Antia (1997) based on their helioseismological analysis. In support of the larger uncertainty used in this paper, we note that the difference between the Grevesse & Noels (1993) values of $Z/X = 0.0230$ is 1 σ according to equation (12).

We include for the first time in this series of papers the uncertainty in the small ^{17}F neutrino flux due to the uncertainty in the measured S_0-factor for the reaction ^{16}O(p, γ)^{17}F. We use the 1 σ uncertainty 18.1% estimated by Adel-

[6] http://www.sns.ias.edu/~jnb/SNdata/sndata.html.

berger et al. (1998). It was an oversight not to include this uncertainty in our previous calculations.

The only flux for which we do not quote an estimated uncertainty is the *hep* flux (see Table 7). The difficulty of calculating from first principles the nuclear cross section factor $S_0(hep)$ is what has caused us not to quote in this series of papers an uncertainty in the *hep* flux (see discussion in Bahcall 1989; Bahcall & Krastev 1998). The *hep*-reaction is uniquely difficult to calculate among the light-element fusion reactions since the one-body and two-body contributions to the reaction rate are comparable in magnitude but opposite in sign, so that the net result is sensitive to a delicate cancellation. Also, two-body axial currents from excitations of Δ isobars are model dependent. In addition, the calculated rate is sensitive to small components in the wave function, particularly *D*-state admixtures generated by tensor interactions. These complications have been discussed most recently and most thoroughly by Marcucci et al. (2000b).

The calculated errors are asymmetric in many cases. These asymmetries in the uncertainties in the neutrino fluxes and experimental event rates result from asymmetries in the uncertainties of some of the input parameters, for example, the important *pp*, ^{7}Be + *p*, and ^{14}N + *p* fusion reactions and the effect of excited states on neutrino absorption cross sections. To include the effects of asymmetric errors, the code exportrates.f was run with different input representative uncertainties and the different higher (lower) rates were averaged to obtain the quoted upper (lower) limit uncertainties.

5.1.3. *NACRE Charged Particle Fusion Rates*

In order to estimate the systematic uncertainties associated with different treatments of the nuclear fusion reactions, we have constructed a solar model that is the same as the standard model discussed in § 5.1.1, except that we have used the charged particle fusion cross sections recommended in the NACRE compilation (Angulo et al. 1999) rather than the fusion cross sections determined by Adelberger et al. (1998). We will refer to this solar model as the NACRE model.

The low-energy cross section factors, S_0, that are recommended by the NACRE collaboration and by Adelberger et al. (1998) agree within their stated 1 σ uncertainties for all of the fusion reactions that are important for constructing a solar model. The only important solar nuclear reactions for which the NACRE collaboration did not recommend interaction rates are the electron capture reactions that produce the ^{7}Be and the *pep* neutrinos; the NACRE collaboration also did not provide energy derivatives for the cross section factors of the CNO reactions. Wherever the data necessary for computing solar fusion rates were not available in the NACRE compilation, we continued to use the Adelberger et al. (1998) recommended values in computing the NACRE model.

Table 9 gives the calculated neutrino fluxes and capture rates predicted by the NACRE solar model. In all cases, the fluxes for the NACRE solar model agree with the fluxes calculated with the standard solar model to well within the 1 σ uncertainties in the standard model fluxes. The ^{7}Be flux from the NACRE model is 1% larger than for the standard model, and the ^{8}B flux is 8% higher. The chlorine capture rate predicted by the NACRE model is 5% higher than for the standard model; the predicted rates for the NACRE model and the standard model differ by less than 1% for the gallium and lithium experiments.

TABLE 9

NEUTRINOS WITH NACRE REACTION RATES

Source	Flux (10^{10} cm^{-2} s^{-1})	Cl (SNU)	Ga (SNU)	Li (SNU)
pp	$5.96(1.00^{+0.01}_{-0.01})$	0.0	69.8	0.0
pep	$1.39 \times 10^{-2}(1.00^{+0.015}_{-0.015})$	0.22	2.8	9.1
hep	9.4×10^{-7}	0.04	0.1	0.1
^{7}Be	$4.81 \times 10^{-1}(1.00^{+0.10}_{-0.10})$	1.15	34.5	9.1
^{8}B	$5.44 \times 10^{-4}(1.00^{+0.20}_{-0.16})$	6.20	13.1	21.2
^{13}N	$4.87 \times 10^{-2}(1.00^{+0.21}_{-0.17})$	0.08	2.9	2.1
^{15}O	$4.18 \times 10^{-2}(1.00^{+0.25}_{-0.19})$	0.28	4.7	10.3
^{17}F	$5.30 \times 10^{-4}(1.00^{+0.25}_{-0.25})$	0.0	0.1	0.1
Total		$8.0^{+1.4}_{-1.1}$	128^{+9}_{-7}	$52.0^{+6.5}_{-5.9}$

NOTE.—The solar neutrino fluxes and neutrino capture rates that were calculated with the NACRE fusion cross sections (Angulo et al. 1999) are given in the table. The only difference between the model used in this calculation and the standard model, whose fluxes are given in Table 7, is that the Adelberger et al. 1998 fusion cross sections were replaced by the NACRE cross sections for all reactions for which the NACRE collaboration quoted zero-energy cross section factors, S_0. The cross sections for neutrino absorption on chlorine are from Bahcall et al. 1996, the cross sections for gallium are from Bahcall 1997, and the cross sections for ^{7}Li are from Bahcall 1989, 1994.

We conclude that this estimate of the systematic uncertainties due to the relative weights given to different determinations of nuclear fusion cross sections suggests likely errors from this source that are significantly smaller than our quoted 1 σ errors for the standard model neutrino fluxes and event rates (see Table 7). Similar conclusions have been reached by Morel et al. (1999) in an independent investigation (see also Castellani et al. 1997).

5.1.4. *Variant and Deviant Models*

Table 10 compares the calculated neutrino fluxes for the seven variant solar models described in § 4.1 and for the four deficient solar models described in § 4.2 with the fluxes obtained for the standard solar model. The range of the ^{8}B neutrino fluxes among the eight standard-like models (rows 1–8 of Table 10) is only $\pm 7\%$, a factor of 2 or 3 smaller than the uncertainty (due to other sources) in the calculated ^{8}B flux of the standard model (see Table 7). The spread in ^{7}Be flux is $\pm 3\%$; the range in ^{37}Cl and ^{71}Ga rates is ± 0.45 and ± 2 SNU, respectively.

The deviant models listed in Table 10 are all deficient in some important aspect of the physics used in their calculation. The No Diffusion, Old Physics, $S_{34} = 0$, and Mixed models all give such bad agreement with helioseismology (compared to the first seven models) that the comparison with the data cannot be made on the same scale as for the standard-like models (see BPB00). The Old Physics model gives an rms difference between the calculated and measured sound speeds that is more than twice as large as when the standard model is used. For the $S_{34} = 0$ model, the rms discrepancy is 7 times worse in the solar interior than for the standard model; for the No Diffusion model, the disagreement is about 7 times worse averaged over the Sun than for the standard model. The Mixed model is the worst of all; the rms disagreement in the solar core is about 25 times larger than for the standard solar model.

Even if one is willing to consider solar models that predict sound speeds that deviate so drastically from the measured helioseismological values, the four deviant solar

TABLE 10

NEUTRINO FLUXES FROM 12 SOLAR MODELS

Model	*pp* ($\times 10^{10}$)	*pep* ($\times 10^{8}$)	*hep* ($\times 10^{3}$)	^{7}Be ($\times 10^{9}$)	^{8}B ($\times 10^{6}$)	^{13}N ($\times 10^{8}$)	^{15}O ($\times 10^{8}$)	^{17}F ($\times 10^{6}$)	Cl (SNU)	Ga (SNU)
Standard	5.96	1.40	9.3	4.82	5.15	5.56	4.88	5.73	7.7	129
NACRE	5.97	1.39	9.4	4.85	5.54	4.93	4.24	5.39	8.1	129
AS00	5.99	1.41	9.4	4.62	4.70	5.25	4.56	5.33	7.1	126
GN 93	5.94	1.39	9.2	4.88	5.31	6.18	5.45	6.50	8.0	130
Pre-M.S.	5.95	1.39	9.2	4.87	5.29	6.16	5.43	6.47	7.9	130
Rotation	5.98	1.40	9.2	4.68	4.91	5.57	4.87	5.79	7.4	127
Radius$_{78}$	5.94	1.39	9.2	4.88	5.31	6.18	5.45	6.50	8.0	130
Radius$_{508}$	5.94	1.39	9.2	4.88	5.31	6.18	5.45	6.50	8.0	130
No Diffusion	6.05	1.43	9.6	4.21	3.87	4.09	3.46	4.05	6.0	120
Old Physics	5.95	1.41	9.2	4.91	5.15	5.77	5.03	5.92	7.8	130
$S_{34} = 0$	6.40	1.55	10.1	0.00	0.00	6.47	5.64	6.70	0.8	89
Mixed	6.13	1.27	6.2	3.57	4.13	3.04	3.05	3.61	6.1	115

NOTE.—The table lists the calculated neutrino fluxes and event rates for the seven variant solar models that are discussed in § 4.1 and for the four deficient solar models that are discussed in § 4.2 and compares the results with the standard model fluxes. The models in rows 2–8 are all variants on the standard model (row 1). The last four models are deficient in some important aspect of the physics used in their construction and do not provide good fits to the helioseismological data.

models do not describe well the solar neutrino data. For the Old Physics, No Diffusion, and Mixed solar models, the predicted rates for the gallium experiments lie between 115 and 130 SNU, which is to be contrasted with the observed rate of 75 ± 5 SNU, which is at least an 8 σ discrepancy. For the $S_{34} = 0$ model, the predicted rate in the chlorine experiment is 0.79 SNU, which is also about 8 σ less than the observed value, 2.56 ± 0.23 SNU.

5.2. *The Electron Number Density*

The probability of converting an electron-type neutrino to a muon or tau neutrino in the Sun depends upon the profile of the electron number density as a function of solar radius. For particular values of the electron density, neutrino energy, and neutrino mass, neutrinos can be resonantly converted from one type of neutrino to another. The Mikheyev-Smirnov resonance occurs if the electron density at a radius r satisfies

$$\frac{n_{e,\mathrm{res}}(r)}{N_{\mathrm{A}}} \approx 66 \cos 2\theta_V \left(\frac{|\Delta m^2|}{10^{-4}\ \mathrm{eV}}\right)\left(\frac{10\ \mathrm{MeV}}{E}\right), \qquad (13)$$

where n_e is the electron number density measured in cm^{-3}, N_{A} is Avogadro's number, θ_V is the neutrino mixing angle in vacuum, $|\Delta m^2|$ is the absolute value of the difference in neutrino masses between two species that are mixing by neutrino oscillations, and E is the neutrino energy.

Figure 8 and Table 11 give the electron number density as a function of solar radius for the standard solar model (BP2000). A much more extensive numerical file of the electron number density versus radius is available on-line (see footnote 4 for the URL); this file contains the computed values of the electron number density at 2493 radial shells.

We see from Figure 8 that for typical values of the neutrino parameters that allow the so-called LMA and SMA MSW solutions that fit all of the currently available solar neutrino data (e.g., Bahcall, Krastev, & Smirnov 1998), the experimentally most important ^{8}B neutrinos ($E \geq 5$ MeV) satisfy the resonance condition, equation (13), at radii that are smaller than the radius of the convective zone. For the so-called LOW MSW solutions and for all MSW solutions with $\theta_V \sim \pi/4$, the resonance radius falls in the outer part of the Sun.

We have not previously published accurate values for the electron density in the outer parts of the Sun, $r \geq 0.8\ R_{\odot}$. The straight line in Figure 8 is an approximation to the electron number density in the standard solar model of Bahcall & Ulrich (1988) (see Bahcall 1989). This approximation, which has been used for over a decade by different groups analyzing solar neutrino data, is

$$\frac{n_e}{N_{\mathrm{A}}} = 245 \exp\left(-10.54\,\frac{R}{R_{\odot}}\right) \mathrm{cm}^{-3}\ . \qquad (14)$$

Figure 8 shows that the approximation given in equation (14) fails badly in the outer regions of the Sun. Recently, several different analyses have been published using the electron number density shown in Figure 8 [or, more precisely, the computer file for $n_e(r)$, which is available on-line (see footnote 4 for the URL)].

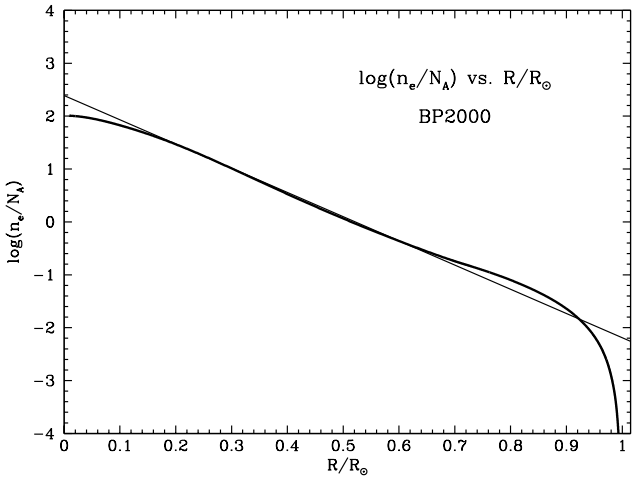

FIG. 8.—Electron number density, n_e, vs. solar radius for the standard solar model (BP2000). The straight-line fit shown is an approximation, eq. (14), given by Bahcall (1989). Eq. (14) has been used previously in many analyses of matter effects on solar neutrino propagation. Precise numerical values for n_e are available on-line. [*See the electronic edition of the Journal for a color version of this figure.*]

TABLE 11

ELECTRON NUMBER DENSITY VERSUS RADIUS FOR THE STANDARD SOLAR MODEL

$R/R_\odot$	log (n_e/N_A)	$R/R_\odot$	log (n_e/N_A)
0.01.....	2.008E+00	0.55.....	−1.527E−01
0.05.....	1.956E+00	0.60.....	−3.605E−01
0.10.....	1.827E+00	0.65.....	−5.585E−01
0.15.....	1.662E+00	0.70.....	−7.428E−01
0.20.....	1.468E+00	0.75.....	−9.098E−01
0.25.....	1.249E+00	0.80.....	−1.099E+00
0.30.....	1.012E+00	0.85.....	−1.330E+00
0.35.....	7.687E−01	0.90.....	−1.642E+00
0.40.....	5.269E−01	0.95.....	−2.164E+00
0.45.....	2.914E−01	1.00.....	−6.806E+00
0.50.....	6.466E−02	...	...

NOTE.—The tabulated values are log (n_e/N_A), where n_e is measured in number per cm^3 and N_A is Avogadro's number. A more extensive numerical file of n_e, containing electron number densities at 2493 radial shells, is available at http://www.sns.ias.edu/~jnb.

TABLE 12

STERILE NUMBER DENSITY, $n_{sterile}$, VERSUS RADIUS FOR THE STANDARD SOLAR MODEL

$R/R_\odot$	log (n_e/N_A)	$R/R_\odot$	log (n_e/N_A)
0.01.....	1.885E+00	0.55.....	−1.901E−01
0.05.....	1.853E+00	0.60.....	−3.978E−01
0.10.....	1.757E+00	0.65.....	−5.956E−01
0.15.....	1.611E+00	0.70.....	−7.777E−01
0.20.....	1.425E+00	0.75.....	−9.436E−01
0.25.....	1.209E+00	0.80.....	−1.133E+00
0.30.....	9.731E−01	0.85.....	−1.364E+00
0.35.....	7.303E−01	0.90.....	−1.676E+00
0.40.....	4.887E−01	0.95.....	−2.198E+00
0.45.....	2.536E−01	1.00.....	−6.839E+00
0.50.....	2.701E−02	...	...

NOTE.—The tabulated values are log $(n_{sterile}/N_A)$, where $n_{sterile}$ is measured in number per cm^3 and N_A is Avogadro's number. A more extensive numerical file of $n_{sterile}$, containing values of $n_{sterile}$ at 2499 radial shells, is available at http://www.sns.ias.edu/~jnb.

5.3. *The Number Density of Scatterers of Sterile Neutrinos*

The effective density of particles for interacting with sterile (right-handed) neutrinos is not the electron number density discussed in the previous subsection, but rather $n_{sterile}$ (see Mikheyev & Smirnov 1986; Lim & Marciano 1988; Barger et al. 1991), where

$$n_{sterile} = n_e - 0.5 n_{neutrons} \quad (15)$$

and $n_{neutrons}$ is the number density of neutrons. Since nearly all of the neutrons in the Sun are either in ^{4}He or in heavier elements with $Z \simeq A/2$, it is easy to derive an analytic expression that relates $n_{sterile}$ and n_e. One obtains

$$n_{sterile} = n_e \left[\frac{1 + 3X}{2(1 + X)} \right]. \quad (16)$$

Figure 9 and Table 12 give the radial distribution of $n_{sterile}$ in the standard solar model. The functional form of $n_{sterile}(r)$ is similar to the functional form of $n_e(r)$. The straight line in Figure 9 is given by an equation of the same form as equation (14) that describes $n_e(r)$ except that the coefficient for $n_{sterile}/N_A$ is 223 (instead of 245 for n_e/N_A).

The number density $n_{sterile}$ is about 25% smaller than the electron number density, n_e, in the center of the Sun, where helium is most abundant. In the central and outer regions of the Sun, $n_{sterile}$ is about 9% less than n_e. Since the slopes of the straight-line fitting functions are the same in Figures 8 and 9, the neutrino survival probabilities are the same for sterile and for active neutrinos as long as the adiabatic approximation is valid (see, e.g., § 9.2 of Bahcall 1989).

5.4. *Neutrino Fluxes as a Function of Solar Age*

Figure 10 shows the most important solar neutrino fluxes, the *pp*, ^{7}Be, ^{8}B, and ^{13}N fluxes, as a function of solar age. The fluxes displayed in the figure were computed using the standard model and are normalized by dividing each flux by its value at the present epoch, labeled by the word "today" in the figure (see Fig. 10 of Guenther & Demarque 1997 for a similar figure plotted on a logarithmic scale).

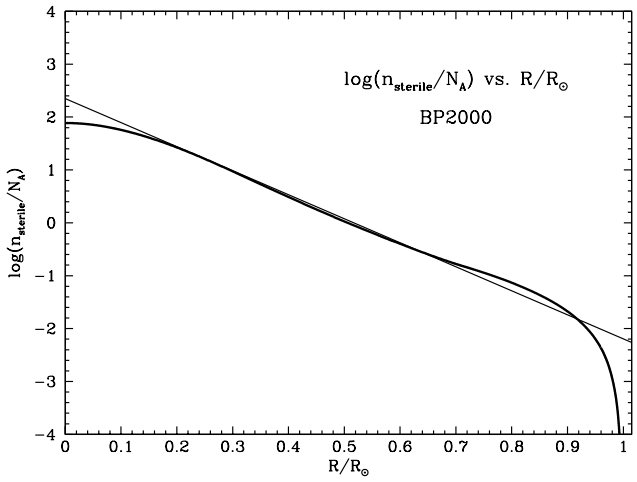

FIG. 9.—Number density, $n_{sterile}$, of scatterers of sterile neutrinos vs. solar radius for the standard solar model (BP2000). The straight line in Fig. 9 is given by an equation of the same form as eq. (14) except that the coefficient for $n_{sterile}/N_A$ is 223 (instead of 245 for n_e/N_A). [*See the electronic edition of the Journal for a color version of this figure.*]

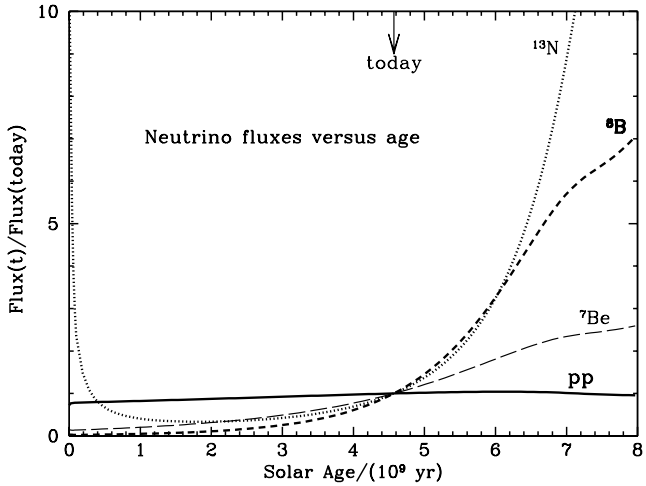

FIG. 10.—*pp*, ^{7}Be, ^{8}B, and ^{13}N neutrino fluxes as a function of solar age. The figure shows the standard model ratios of the fluxes divided by their values at 4.57×10^9 yr. The *pp* flux is represented by a solid line, the ^{7}Be flux by a long-dashed line, the ^{8}B flux by a short-dashed line, and the ^{13}N flux by a dotted line. [*See the electronic edition of the Journal for a color version of this figure.*]

The *pp* flux is relatively constant over the entire 8×10^9 yr shown in Figure 10. At the beginning of its lifetime, the *pp* flux is about 75% of its current value and reaches 90% of its present value after 2.6×10^9 yr. At the current epoch, the flux is changing very slowly, about 4% per 10^9 yr. The *pp* flux reaches a maximum, 4% larger than its current value, at a solar age of 6.0×10^9 yr and then declines slowly and steadily to 96% of its present value at an age of 8×10^9 yr.

The ^{7}Be and ^{8}B neutrino fluxes increase monotonically and by larger amounts than the *pp* flux. Both the ^{7}Be and the ^{8}B fluxes begin with very low fluxes relative to their current values, 14% and 3%, respectively, of their intensities at 4.57×10^7 yr. At a solar age of 8×10^9 yr, the ^{7}Be neutrino flux is 2.6 times larger than it is today and the ^{8}B neutrino flux is 7.1 times larger than today. At the current epoch, the ^{7}Be flux is increasing by about 65% per 10^9 yr and the ^{8}B flux is increasing faster, about 120% per 10^9 yr.

The ^{13}N neutrino flux has the most interesting time dependence. In the first 10^8 yr on the main sequence, the ^{13}N flux is much larger than its current value because ^{12}C has not yet been burned to the equilibrium value appropriate for the CNO cycle. The reaction $^{12}C(p, \gamma)^{13}N$ occurs relatively often in this early stage of solar evolution, and the neutrino flux from ^{13}N beta decay has a peak value of about 11 times its current flux. The minimum ^{13}N flux, 33% of its present value, is attained at a solar age of 1.8×10^9 yr. Thereafter, the ^{13}N flux increases steadily as the central temperature of the solar model increases and reaches an intensity of 18 times its current value at a solar age of 8×10^9 yr.

6. SOUND SPEEDS

Section 6.1 presents a panoramic view of the predicted standard model sound speeds and compares the observations and the calculations on a scale that is relevant for interpreting solar neutrino experiments. In § 6.2 we compare on a zoomed-in scale the standard model calculations with the results of six helioseismological measurements. The zoomed-in scale used in this subsection can reveal fractional discrepancies between calculations and observations that are smaller than 0.1%. In § 6.3 we consider a particular solar model that includes rotation in a plausible way. This model smooths the composition discontinuity at the base of the convective zone, which locally improves the agreement with the measured sound speeds but worsens the overall rms agreement (within the uncertainties allowed by input data). For neutrino emission, the predictions of the rotation model are not significantly different from the standard model predictions.

Some authors (see, e.g., Guenther & Demarque 1997) compare their solar models directly with the *p*-mode oscillation frequencies rather than with inverted quantities such as the sound speed. The reader is referred to Guenther & Demarque (1997) for a discussion of the direct comparison method, its application, and additional references.

We have chosen to use the sound speed profile because the inversion process that produces the inferred sound speeds allows one to remove the uncertainties, common to all *p*-mode oscillation frequencies, that arise from the near-surface regions of the Sun. These common uncertainties are due to the treatment of convection, turbulence, and nonadiabatic effects. Inversion techniques are designed to minimize the effects of these outer layers (see, e.g., Basu et al. 1996). Moreover, the sound speed profile summarizes in a robust way the results obtained for many thousands of oscillation frequencies. Finally, the inversion procedure allows one to isolate different regions of the Sun, which is important in the context of discussions regarding solar neutrinos. The neutrinos are produced deep in the solar interior. In BPB00, we have discussed in detail the systematic uncertainties and assumptions related to the inversion for the sound speeds and for the less accurately determined density.

6.1. *Sounds Speeds: Panoramic View*

Figure 11 shows the fractional differences between the calculated sound speeds for the standard model and what may be the most accurate available sound speeds measured by helioseismology, the LOWL1+BiSON measurements presented in Basu et al. (1997). These sound speeds are derived from a combination of the data obtained by the Birmingham Solar Oscillation Network (BiSON; see Chaplin et al. 1996) and the Low-ℓ instrument (LOWL; see Tomczyk, Schou, & Thompson 1995a; Tomczyk et al. 1995b).

The rms fractional difference between the calculated and the measured sound speeds is 10.4×10^{-4} over the entire region in which the sound speeds are well measured, $0.05 \leq r \leq 0.95\ R_\odot$. In the solar core, $0.05 \leq r \leq 0.25\ R_\odot$ (in which about 95% of the solar energy and neutrino flux are produced in a standard solar model), the rms fractional difference between measured and calculated sound speeds is 6.3×10^{-4}. The standard model sound speeds agree with the measured sound speeds to 0.1% whether or not one limits the comparison to the solar interior or averages over the entire Sun. Systematic uncertainties $\sim 3 \times 10^{-4}$ are contributed to the sound speed profile by each of three sources: the assumed reference model, the width of the inversion kernel, and the measurement errors (see BPB00).

The vertical scale of Figure 11 was chosen so as to include the arrow marked "^{7}Be lowered (1 σ off Ga)." This

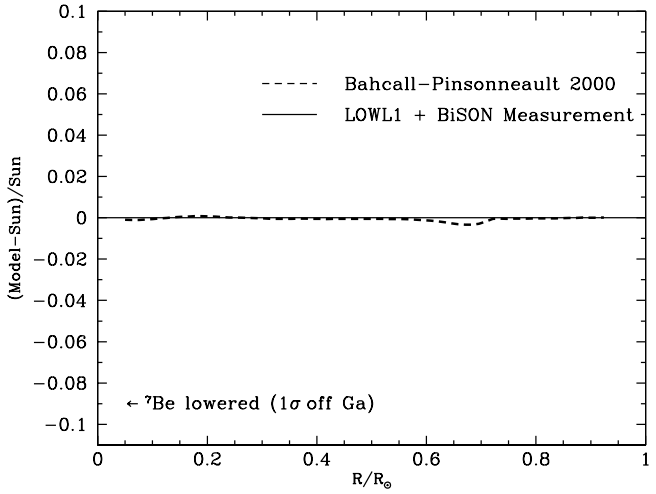

FIG. 11.—Predicted vs. measured sound speeds. The figure shows the excellent agreement between the calculated sound speeds for the standard solar model (BP2000) and the helioseismologically measured (Sun) sound speeds. The horizontal line at 0.0 represents the hypothetical case in which the calculated sound speeds and the measured sound speeds agree exactly everywhere in the Sun. The rms fractional difference between the calculated and the measured sound speeds is 0.10% for all solar radii between 0.05 and 0.95 $R_\odot$ and is 0.08% for the deep interior region, $r \leq 0.25\ R_\odot$, in which neutrinos are produced. [*See the electronic edition of the Journal for a color version of this figure.*]

arrow indicates the typical difference between solar model speeds and helioseismological measurements that would be expected if the discrepancy between the gallium solar neutrino measurements and the predictions in Table 7 were due to errors in the solar physics of the standard solar model (see discussion in BBP98).

Figure 12 and Table 13 give the sound speeds versus the solar radius that are calculated using the standard solar model. The sound speed declines from about 500 km s^{-1} in the solar core to about 100 km s^{-1} at 0.95 $R_\odot$. An extensive table of the standard model sound speeds is available on-line (see footnote 4 for the URL).

6.2. *Sounds Speeds: Zoom in*

Figure 13 compares the results of six precise observational determinations of the solar sound speed with the results of our standard solar model. The vertical scale has been expanded by a factor of 21 relative to Figure 11 in order to show the small but robust discrepancies between the calculations and the observations and to indicate the size of the differences between the various measurements. In the deep solar interior where neutrinos are produced, $R/R_\odot \leq 0.25$, the differences between the various observational determinations of the sound speed are comparable to the differences between BP2000 and any one of the measured sets of sound speeds.

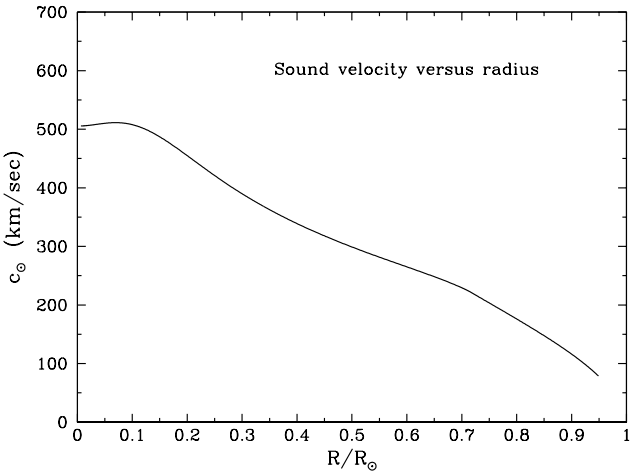

FIG. 12.—Calculated solar sound speed vs. radius for the standard solar model, BP2000. To an accuracy of about 0.5 km s^{-1} the calculated and the observed sound speeds are the same (see Figs. 13 and 14). [*See the electronic edition of the Journal for a color version of this figure.*]

TABLE 13

SOUND SPEED AS A FUNCTION OF RADIUS FOR THE STANDARD SOLAR MODEL

R ($R_\odot$)	c_s (100 km s^{-1})	R ($R_\odot$)	c_s (100 km s^{-1})
0.01.....	5.057	0.50.....	2.990
0.05.....	5.101	0.55.....	2.817
0.10.....	5.078	0.60.....	2.651
0.15.....	4.870	0.65.....	2.483
0.20.....	4.550	0.70.....	2.295
0.25.....	4.210	0.75.....	2.035
0.30.....	3.898	0.80.....	1.761
0.35.....	3.627	0.85.....	1.476
0.40.....	3.389	0.90.....	1.162
0.45.....	3.179	0.95.....	0.778

NOTE.—The sound speeds are given in units of 100 km s^{-1}.

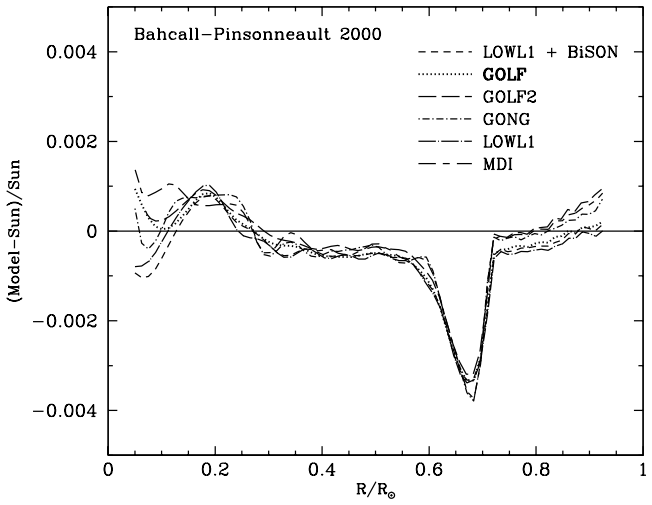

FIG. 13.—Six precise helioseismological measurements vs. BP2000. The figure compares the fractional difference between the sound speeds calculated for the standard solar model (BP2000) and the sound speeds in six helioseismological experiments. The references to the helioseismological data are given in the text. Systematic uncertainties due to the assumed reference model and the width of the inversion kernel are each ~ 0.0003 (see BPB00). [*See the electronic edition of the Journal for a color version of this figure.*]

The *p*-mode frequencies used in deriving the observed sound speeds shown in Figure 13 were obtained from a number of different sources. In addition to the LOWL1 + BiSON data described in § 6.1, we have used data from a number of other sources. (1) Data from the first year of LOWL observations. The sound speed inversions are described in Basu et al. (1997) and are referred to as LOWL1 in this paper. (2) Data from the Michelson Doppler Imager (MDI) instrument on board the *Solar and Heliospheric Observatory* (*SOHO*) during the first 144 days of its operation (see Rhodes et al. 1997). The results of the sound speed inversions using these data are from Basu (1998). (3) The frequencies obtained from the data obtained by the Global Oscillation Network Group (GONG) between months 4 and 14 of its observations. The solar sound speeds are from Basu (1998). (4) Initial observation taken by the Global Oscillations at Low Frequencies (GOLF) instrument on board *SOHO*, combined with intermediate data from MDI. We have labeled the sound speeds obtained as GOLF1, and the solar sound speed results can be found in Turck Chièze et al. (1997). (5) More recent data from GOLF (Thiery et al. 2000), combined with intermediate-degree data obtained from the first 360 days of observations by the MDI instrument (Schou et al. 1997). The sound speed results are described in Basu et al. (2000). These results have been labeled as GOLF2.

There are other helioseismological data sets that could have been used. Of these, the data by Toutain et al. (1998) may be the most relevant. This data set has been discussed extensively in Basu et al. (2000). Toutain et al. (1998) were the first to show the effect of line profile asymmetry on low-degree modes. The sound speed inversions in their

paper were, however, very different from what had been obtained previously. Basu et al. (2000) showed that this difference results primarily from the two modes, $l = 2, n = 6$ and $l = 2, n = 7$, whose frequencies (and errors on the frequencies) were suspect. In a later paper, Bertello et al. (2000b) confirmed most of the low-frequency modes in the Toutain et al. (1998) data set, but not the two questionable modes. Additionally, they determined the frequencies of some very low frequency low-degree modes. The sound-speed inversion results of Bertello et al. (2000b) are similar to those in Basu et al. (2000) and have similar errors in the inversion results over most of the solar interior. However, inversions using data from Bertello et al. (2000a, 2000b) show that in the inner 2% of the Sun the errors are smaller than those in the inversions of Basu et al. (2000). The main effect of the new data is that it allows us to probe slightly deeper into the core (0.064 $R_\odot$ as opposed to 0.070 $R_\odot$).

The MDI and GONG sets have good coverage of intermediate-degree modes. The MDI set has *p*-modes from $\ell = 0$ up to a degree of $\ell = 194$, while the GONG set has modes from $\ell = 0$ up to $\ell = 150$. However, both these sets are somewhat deficient in low-degree modes. The LOWL1 + BiSON combination, on the other hand, has a better coverage of low-degree modes but has modes from $\ell = 0$ only up to $\ell = 99$. The GOLF data sets only contain low-degree modes ($l = 0, 1, 2$) and hence have to be combined with other data before they can be used to determine the solar sound speed profile.

Figure 14 shows the somewhat less precise agreement that was obtained between BBP98 and the helioseismological data. The BBP98 model and the observed sound speeds agree in the solar interior to about the same accuracy as for BP2000 and the observed speeds. However, the BBP98 model sound speeds are about 0.1% smaller than the observed speeds in the broad intermediate region between $0.3R/R_\odot$ and $0.7R/R_\odot$ (see Figs. 13 and 14). Averaged over the entire region over which good measurements are available, 0.05–0.95 $R_\odot$, the rms fractional difference between the BBP98 model and the LOWL1 + BiSON sound speeds is 13×10^{-4}, which should be compared with an rms difference of 10.4×10^{-4} for the BP2000 model (see § 6.1).[7]

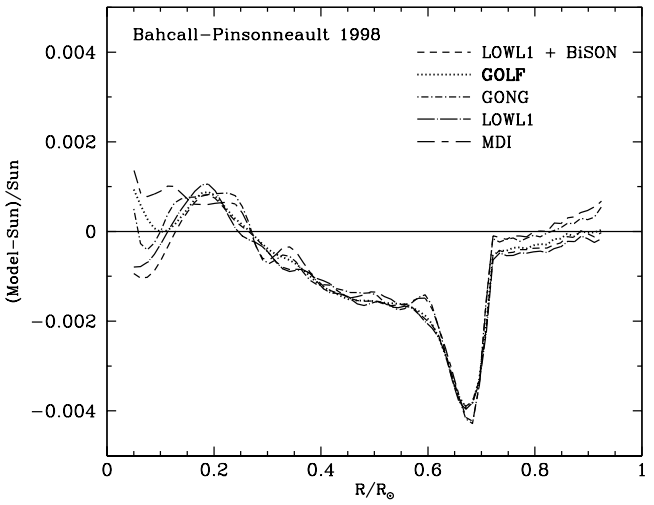

FIG. 14.—Five precise helioseismological measurements vs. BBP98. The figure compares the fractional difference between the sound speeds calculated for the 1998 standard solar model (BBP98) and the sound speeds in five helioseismological experiments. The references to the helioseismological data are given in the text. (The GOLF2 data were not available when this comparison was originally made.) The rms fractional difference between the calculated and the measured sound speeds is 0.13% for all solar radii between 0.05 and 0.95 $R_\odot$. [*See the electronic edition of the Journal for a color version of this figure.*]

In BBP98, we speculated that the broad feature of disagreement at the 0.1% level in Figure 14 might be due to a combination of small errors in the adopted radiative opacities or in the equations of state. We investigated the implications for solar neutrino fluxes of the possibility that the small, broad discrepancy was due to an opacity error and concluded that if this were the case, then the corrected solar model would predict ^{7}Be and ^{8}B neutrino fluxes that are about 5% larger than the fluxes predicted by BBP98.

Indeed, the origin of the broad discrepancy is due to an error in interpolating the radiative opacity near the edges of the opacity tables, as explained in § 2.1. The effect on the neutrino fluxes is somewhat smaller than we had estimated, an increase (relative to BBP98) of 2% for ^{7}Be neutrinos and 3% for ^{8}B (see the results for GN93 in Table 7 and Table 1 of BBP98).

6.3. *Sounds Speeds: Rotation*

Figure 15 compares the sound speeds of the Rotation model with the six precise observed sets of sound speeds. In the region between 0.3 and 0.6 $R_\odot$, the agreement between the Rotation model and the helioseismological data is slightly less good than with the standard solar model (compare Figs. 13 and 15). Quantitatively, over the entire region between 0.05 and 0.95 $R_\odot$, the rms fractional difference between the Rotation model and the LOWL1 + BiSON sound speeds is 12×10^{-4}, which is to be compared with 10×10^{-4} for BP2000. In the solar core (≤ 0.25 $R_\odot$), the two models, Rotation and BP2000, have almost identical rms fractional differences with respect to the LOWL1 + BiSON sound speeds, 0.073% and 0.0064%, respectively.

Figure 16 compares both the Rotation and the standard model with just the LOWL1 + BiSON sound speeds. This figure shows that the Rotation model gives marginally better agreement with the measured sound speeds right at the base of the convective zone, comparable agreement in the deep interior, $r \leq 0.25$ $R_\odot$, and slightly less good agreement in the intermediate region between 0.3 and 0.6 $R_\odot$.

The neutrino fluxes calculated with the Rotation model lie well within the estimated errors in the standard model fluxes, as can be seen easily by comparing the fluxes and the errors given in Tables 7 and 10. The ^{7}Be flux for the Rotation model is 3% less than the standard model ^{7}Be, and the

[7] The standard model described in this paper differs from the BBP98 model in two respects, both discussed in § 2.1, that are significant for helioseismology: the correction of the opacity interpolation error and the slightly different heavy-element mixture adopted for the BP2000 model. For helioseismology, the only significant difference between GN93 and BBP98 is the correction of the interpolation error; the heavy-element abundances used for both models are the same (with $Z/X = 0.0245$). When a figure like Fig. 13 was constructed using GN93 instead of BP2000, the general form of the small differences was practically the same. In fact, the rms difference averaged over the whole Sun between GN93 and LOWL1 + BiSON is 0.00086, which is slightly better than the value of 0.00104 for BP2000 vs. LOWL1 + BiSON. One therefore obtains the correct impression by comparing Figs. 13 and 14.

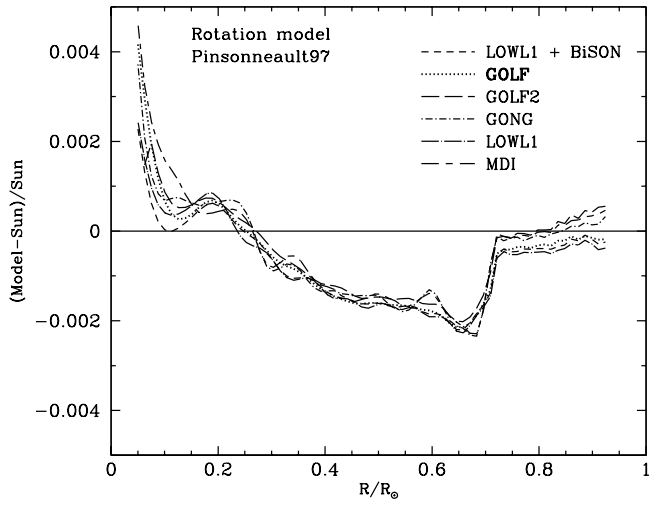

FIG. 15.—Six precise helioseismological measurements vs. the Rotation model. The figure compares the fractional difference between the sound speeds calculated for the rotational solar model and the sound speeds in six helioseismological experiments. The model was developed by Pinsonneault and collaborators to explain the depletion of lithium. The references to the helioseismological data are given in the text. [*See the electronic edition of the Journal for a color version of this figure.*]

TABLE 14

HELIUM ABUNDANCE AND THE DEPTH OF THE CONVECTIVE ZONE

Model	Y_s	R(CZ)
Standard	0.244	0.714
NACRE	0.244	0.713
AS00	0.239	0.714
GN93	0.245	0.712
Pre-MS	0.246	0.713
Rotation	0.248	0.714
Radius$_{-78}$	0.245	0.712
Radium$_{-508}$	0.245	0.712
No Diffusion	0.266	0.726
Old Physics	0.248	0.712
$S_{34} = 0$	0.242	0.715
Mixed	0.254	0.732
Measured	0.249 ± 0.003	0.713 ± 0.001

NOTE.—The calculated present-day helium abundance on the surface and the convective zone depth are given for 11 solar models discussed in this paper. The quoted errors in the measured values of Y and R(CZ) represent best estimates of the systematic uncertainties but cannot be interpreted rigorously in terms of 1 or 3 σ errors.

^{8}B flux is 5% lower than the corresponding standard model value. The Rotation model predicts a capture rate by ^{37}Cl that is 0.3 SNU less than the standard model rate and a ^{71}Ga capture rate that is 2 SNU less than the standard model rate.

7. HELIUM ABUNDANCE AND DEPTH OF THE CONVECTION ZONE

Table 14 gives the calculated present-epoch values for the depth of the convective zone, R(CZ), and the surface helium abundance, Y_s, for all 11 of the solar models considered in this paper.

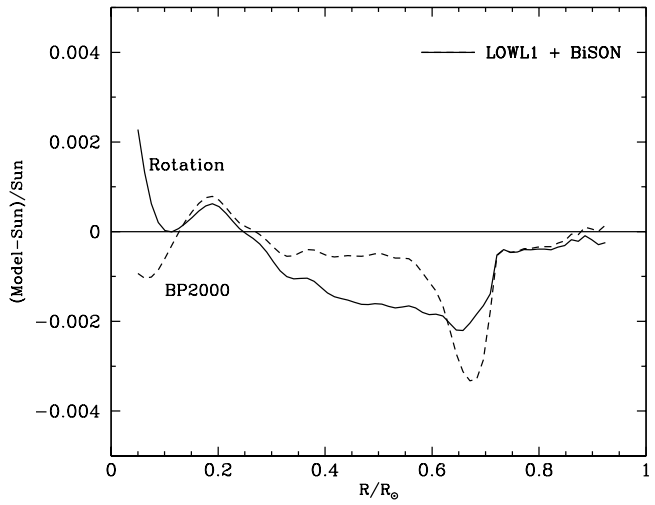

FIG. 16.—BP2000 vs. the Rotation model. The figure compares the fractional difference between the sound speeds determined from the LOWL1+BiSON data with the sound speeds calculated for the BP2000 solar model and the rotational solar model. The BP2000 model agrees slightly better with the measured sound speeds in the intermediate region between 0.3 and 0.6 $R_\odot$. [*See the electronic edition of the Journal for a color version of this figure.*]

The observed values determined using measurements of p-modes are $R(\mathrm{CZ}) = (0.713 \pm 0.001)\ R_\odot$ (Basu & Antia 1995; for earlier work see Christensen-Dalsgaard, Gough, & Thompson 1991) and $Y_s = 0.249 \pm 0.003$ (Basu & Antia 1997; see also Richard et al. 1996).

The quoted errors are systematic; the statistical uncertainties are much smaller. For example, the cited uncertainty for Y_s is designed to span the two values obtained when using two different equations of state (see Basu & Antia 1997). There is no rigorous way of establishing a confidence level based upon agreement within, for example, 1 or 2 times the estimated systematic uncertainty. We point out that the recent reassessment of Z/X by Grevesse & Sauval (1998) resulted in a value of $Z/X = 0.0230$, which differs from the helioseismologically recommended value of $Z/X = 0.0245 \pm 0.0008$ by twice the quoted uncertainty of the helioseismological determination.

As a rule of thumb, we shall regard agreement within 2 times the quoted systematic uncertainty as "satisfactory" and agreement within 1 times the quoted systematic uncertainty as "excellent."

Nine of the 11 solar models considered in this paper give excellent or satisfactory agreement with the observed depth of the convective zone. The only exceptions to the good agreement with the measured convective zone depth are the No Diffusion and the Mixed models, which are both strongly disfavored by the helioseismological measurements.

The No Diffusion, $S_{34} = 0$, and AS00 models are the only ones that are not within twice the quoted uncertainty in the measured surface helium abundance. The No Diffusion model yields a surface helium abundance that is more than 5 times the quoted uncertainty away from the helioseismological measurement, which very strongly disfavors the No Diffusion model. The surface helium abundance calculated for the AS00 model is also rather far from the helioseismological value, more than 3 times the quoted uncertainty in the helioseismological determination. This discrepancy should be examined more fully in future years as the abundance determinations are refined, the helio-

seismological determination of the helium abundance is repeated, and the input data to the helioseismological analysis are varied over a wide range of allowed possibilities.

8. DISCUSSION AND SUMMARY

This paper provides new information about four topics: (1) the characteristics of the standard solar model at the current epoch (§ 8.1), (2) time dependences of important characteristics of the standard solar model (§ 8.2), (3) neutrino fluxes and related quantities for standard and variant solar models (§ 8.3), and (4) measured versus calculated solar sound speeds (§ 8.4). Extensive numerical data that are useful for applications are available on-line (see footnote 4 for the URL).

Just for fun, we provide our favorite list, our "top three," among the many disparate results presented in this paper. Our top three results are listed in § 8.5.

8.1. *Standard Solar Model: Current Epoch*

We present detailed numerical tabulations of the computed characteristics of our standard solar model, which is defined and discussed in § 2. These tables include, as a function of the solar radius, the enclosed mass fraction, temperature, mass density, electron number density, pressure, and luminosity fraction created in a given spherical shell, as well as the mass fractions of ^{1}H, ^{3}He, ^{4}He, ^{7}Be, ^{12}C, ^{14}N, and ^{16}O. Over the years, previous numerical versions of our standard model have been used for a variety of purposes that range from comparisons with other stellar evolution codes, estimating the importance in the Sun of newly considered physical effects, searching for possible instabilities in the Sun, comparison with helioseismological measurements, and the calculation of processes (especially the MSW effect) that influence the propagation of solar neutrinos.

In the past we have published in hard copy form increasingly more detailed and precise numerical tables of the characteristics of the solar interior. The capabilities of current calculations and the requirements of some of the most interesting applications have made complete hard copy publication no longer appropriate. We have therefore limited ourselves in § 2 to describing briefly the ingredients we use in calculating the current standard model. We present the numerical results in exportable data files that are available on-line (see footnote 4 for the URL).

8.2. *Standard Solar Model: Time Dependences*

For the first time in this series of papers, we have focused, especially in § 3, on details of the time dependence of important characteristics of the standard solar model.

The total luminosity in the standard model increases by 48% from the zero-age main-sequence stage to the present epoch. Over the same period, the effective temperature varies by only $\pm 1.3\%$. These predictions constitute constraints on models for the evolution of Earth.

The predicted time evolution of the solar luminosity is robust. Figure 2 shows that all solar models, even those models with deficient physics that are strongly disfavored by helioseismological measurements, predict essentially the same luminosity evolution. The average rms deviation of the deviant models, the Mixed, No Diffusion, and $S_{34} = 0$ models, from the standard solar model luminosity is only 1% over the history of the Sun from 1 Gyr to the current epoch (see § 3.1 for more details).

Table 4 presents the calculated large and small separations of the p-mode frequencies as a function of age for the standard solar model.

We have presented in § 3 the time evolution of some of the principal physical quantities characterizing the solar core (the central temperature, density, pressure, and hydrogen mass fraction, as well as the fractions of the solar luminosity generated by different nuclear reactions). We also present the evolution of important quantities at the base of the convective zone (radiative opacity, temperature, density, and pressure). We hope that these data and the scaling relations we have inferred will be sufficient to permit a future physical understanding of the time dependences using analytic and semianalytic arguments.

We find some simple scaling relations. For example, the solar luminosity, $L_\odot(t)$, is approximately related to the solar radius, $R_\odot(t)$, as $L_\odot(t) \propto R_\odot(t)^{2.5}$. The depth of the convective zone, $R(\mathrm{CZ}, t)$, scales as $R(\mathrm{CZ}, t) \propto R_\odot(t)$, and the central temperature, $T_c(t)$, shows a similar behavior, $T_c(t) \propto R_\odot(t)$. Moreover, we find that the mass of the convective zone, $M(\mathrm{CZ}, t)$, satisfies $M(\mathrm{CZ}, t) \propto R_\odot(t)^{-2}$. The effective temperature is approximately constant, varying by only $\pm 0.7\%$ from a solar age of 2×10^9 to 8×10^9 yr.

These results make predictions that are potentially testable. In principle, the measurement of the luminosity (by astrometry) of a star with the same mass and chemical composition (Z/X) as the Sun would allow the prediction of the star's effective temperature, the depth and mass of the convective zone, and the large and small separations of the p-mode frequencies (see, e.g., Monteiro, Christensen-Dalsgaard, & Thompson 2000; Christensen-Dalsgaard 1997). In practice, it is difficult to make measurements sufficiently accurately to make possible precise tests of stellar evolution theory. For an appraisal of both the potential and the difficulty of making such measurements, the reader is referred to Guenther & Demarque (2000) and Morel et al. (2000b) on the binary pair of approximately solar mass stars, α Centauri AB (1.1 and 0.9 $M_\odot$).

8.3. *Neutrino Fluxes and Related Quantities*

Figure 8 and Table 11 give the electron number density as a function of position in the Sun for the standard solar model. The distribution of the electron density is required to compute the probability for matter-induced oscillations between active neutrinos. Similarly, Figure 9 and Table 12 give the radial distribution of the number density of scatterers of sterile neutrinos, n_{sterile}, in the standard solar model. We have not previously published precise values for the electron number density, or of n_{sterile}, in the outer regions of the Sun. The outer regions are relevant for large mixing angle neutrino oscillations with relatively low neutrino mass differences ($\Delta m^2 < 10^{-8}$ eV^2).

Table 7 presents the neutrino fluxes and the event rates in the chlorine, gallium, lithium, and electron-scattering neutrino experiments that are predicted by the standard solar model. These predictions assume that nothing happens to solar neutrinos after they are produced. The table also gives estimates of the uncertainties in the fluxes and the event rates; § 5.1 contains a discussion of the physical origin of the uncertainties, as well as the software used to calculate the asymmetric error estimates.

How do the predictions of solar neutrino event rates compare with experiment? Table 8 compares the predictions of BP2000 with the results of the chlorine,

GALLEX+GNO, SAGE, Kamiokande, and Super-Kamiokande solar neutrino experiments. This table assumes that nothing happens to the neutrinos after they are created in the Sun. The standard predictions differ from the observed rates by many standard deviations. Because of an accidental cancellation, the predicted solar neutrino event rates for BP2000 and BBP98 are almost identical (see § 5.1.1).

Table 10 compares the neutrino fluxes and the experimental event rates for all nine of the solar models whose helioseismological properties were investigated in BPB00, plus two additional standard-like models considered here that have somewhat different heavy-element–to–hydrogen ratios. The seven standard-like models (the first seven models in Table 10) all produce essentially the same neutrino predictions; the spreads in the predicted *pp*, ^{7}Be, and ^{8}B fluxes are $\pm 0.7\%$, $\pm 3\%$, and $\pm 6.5\%$, respectively. The calculated rates for the seven standard-like solar models have a range of ± 0.45 SNU for the chlorine experiment and ± 2 SNU for the gallium experiments.

The estimated total errors from external sources (see Table 7), such as nuclear cross section measurements and heavy-element abundances, are about a factor of 3 larger than the uncertainties resulting from the solar model calculations.

We have investigated one possible source of systematic errors, the relative weights assigned to different determinations of nuclear fusion cross sections. We calculated the neutrino fluxes and predicted event rates using the NACRE (Angulo et al. 1999) fusion cross sections rather than the Adelberger et al. (1998) cross sections. The NACRE parameters lead to slightly higher predicted event rates in solar neutrino experiments. However, all changes in the neutrino fluxes and event rates between the NACRE-based predictions and the standard predictions (based upon Adelberger et al. 1998 nuclear parameters) are much less than the 1 σ uncertainties quoted for the standard model (see Tables 7 and 9).

The neutrino event rates predicted by all seven of the standard-like solar models considered here are inconsistent at the 5 σ level (combined theoretical and experimental errors) with the results of the two gallium experiments, GALLEX and SAGE, assuming that no new physics is occurring. The inconsistency with the chlorine experiment is similar but more complex to specify, since the largest part of the theoretical uncertainty in the calculated standard capture rate is due to the electron-type neutrinos from ^{8}B beta decay. The fractional uncertainty in the ^{8}B flux depends upon the magnitude of the flux created in the solar interior. Moreover, the amount by which this ^{8}B flux is reduced depends upon the adopted particle physics scenario.

A similar level of inconsistency persists even for the ad hoc deficient models, such as the $S_{34} = 0$ and Mixed models, that were specially concocted to minimize the discrepancy with the neutrino measurements. For example, the calculated rates for the Mixed model are $6.15^{+1.0}_{-0.85}$ SNU for the chlorine experiment and $115^{+6.8}_{-5.1}$ SNU for gallium experiments. The Mixed model is 4.2 σ below the measured chlorine rate and 6.3 σ below the measured gallium rate. In addition, the deficient models are strongly disfavored by the helioseismology measurements.

Figure 10 shows the calculated time dependence of the *pp*, ^{7}Be, ^{8}B, and ^{13}N solar neutrino fluxes. At the current epoch, the *pp* flux is increasing at a rate of 4% per 10^9 yr, and the ^{7}Be, ^{8}B, and ^{13}N fluxes at the rates of 45%, 90%, and 99% per 10^9 yr, respectively. Since the age of the Sun is estimated to be uncertain by only 5×10^6 yr (see the Appendix by Wasserburg in Bahcall & Pinsonneault 1995), the age of the Sun does not represent a significant uncertainty for solar neutrino predictions.

8.4. *Sound Speeds*

Figure 11 shows the excellent agreement between the helioseismologically determined sound speeds and the speeds that are calculated for the standard solar model. The scale on this figure was chosen so as to highlight the contrast between the excellent agreement found with the standard model and the 2 orders of magnitude larger rms difference for a solar model that could reduce significantly the solar neutrino problems. One would expect characteristically a 9% rms difference between the observations and the predictions of solar models that significantly reduce the conflicts between solar model measurements and solar model predictions. Averaged over the entire Sun, the rms fractional difference is only 0.10% between the standard solar model sound speeds and the helioseismologically determined sound speeds. The agreement is even better, 0.06%, in the interior region in which the luminosity and the neutrinos are produced. Table 13 presents numerical values for the sound speeds predicted by the standard solar model at representative radial positions in the Sun.

All eight of the standard-like solar models considered in this paper give acceptable agreement with the measured depth of the convective zone and the surface helium abundance (see Table 14). Of the 12 standard, standard-like, variant, and deviant solar models considered here, only the No Diffusion and Mixed models disagree strongly with the measured convective zone depth.

There are small but robust discrepancies between the measured and the calculated solar sound speeds. Figure 13 shows the fractional differences between the standard model sound speeds and the speeds measured in each of six different determinations (using *p*-mode data from LOWL1, BiSON, GONG, MDI, GOLF, and GOLF2). The vertical scale for Figure 13 is expanded 21 times compared to the vertical scale of Figure 11. As can be seen from Figure 13, the differences between observed and measured sound speeds are comparable over much of the Sun to the differences between different measurements of the sound speed, but there is a clear discrepancy near the base of the convective zone that is independent of which observational data set is used. There may also be a less prominent discrepancy near 0.2 $R_\odot$.

The agreement between the BP2000 sound speeds and the measured values is improved over what was found earlier with the BBP98 model. This improvement may be seen by comparing Figures 13 and 14. The improvement is striking in the region between 0.3 and 0.7 $R_\odot$ and is due to the correction of an error in the interpolation algorithm for the radiative opacity (see discussion in § 2.1).

The Rotation model includes a prescription for element mixing that was designed to explain the depletion of lithium. The calculated differences between the Rotation and the standard models represent a reasonable upper limit to the effects that rotation, sufficient to explain lithium depletion, might produce. The overall agreement between the sound speeds of the Rotation model and the helio-

seismologically determined sound speeds is slightly worse, 0.12% rather than 0.10%, than the agreement obtained with the standard solar model. The difference between the solar neutrino fluxes predicted by the Rotation model and the standard model is typically about $0.3\sigma_\nu$, where σ_ν represents the uncertainties given in Table 7 for the standard model neutrino fluxes. We conclude that further improvements of the theoretical calculations motivated by refinements of *p*-mode oscillation measurements are unlikely to affect significantly the calculated solar neutrino fluxes.

8.5. *Top Three Results*

Here are our favorite three results in this paper:

1. The robust luminosity evolution of the Sun (see Fig. 2).
2. The excellent agreement of the standard model sound speeds with the measured sound speeds on the scale relevant for solar neutrino discussions (see Fig. 11).
3. The simple relations as a function of time between the solar radius, the solar luminosity, the depth of the convective core, and the mass of the convective core (see eqs. [1]–[5]).

We are grateful to many colleagues in solar physics, nuclear physics, and particle physics for valuable discussions, advice, criticism, and stimulation. J. N. B. is supported in part by NSF grant PHY-0070928.

REFERENCES

Abdurashitov, J. N., et al. 1999, Phys. Rev. C, 60, 055801 (SAGE Collaboration)
Adelberger, E. C., et al. 1998, Rev. Mod. Phys., 70, 1265
Alexander, D. R., & Ferguson, J. W. 1994, ApJ, 437, 879
Angulo, C., et al. 1999, Nucl. Phys. A, 656, 3
Antia, H. M. 1998, A&A, 330, 336
Antia, H. M., & Chitre, S. M. 1999, A&A, 317, 1000
Asplund, M. 2000, A&A, 359, 755
Bahcall, J. N. 1962, Phys. Rev., 128, 1297
———. 1989, Neutrino Astrophysics (Cambridge: Cambridge Univ. Press)
———. 1994, Phys. Rev. D, 49, 3923
———. 1997, Phys. Rev. C, 56, 3391
Bahcall, J. N., Bahcall, N. A., & Shaviv, G. 1968, Phys. Rev. Lett., 20, 1209
Bahcall, J. N., Basu, S., & Pinsonneault, M. H. 1998, Phys. Lett. B, 433, 1 (BBP98)
Bahcall, J. N., Fowler, W. A., Iben, I., & Sears, R. L. 1963, ApJ, 137, 344
Bahcall, J. N., & Glasner, A. 1994, ApJ, 427, 485
Bahcall, J. N., Huebner, W. F., Lubow, S. H., Parker, P. D., & Ulrich, R. K. 1982, Rev. Mod. Phys., 54, 767
Bahcall, J. N., & Krastev, P. I. 1998, Phys. Lett. B, 436, 243
Bahcall, J. N., Krastev, P. I., & Smirnov, A. Yu. 1998, Phys. Rev. D, 58, 096016
Bahcall, J. N., Lisi, L., Alburger, D. E., De Braeckeleer, L., Freedman, S. J., & Napolitano, J. 1996, Phys. Rev. C, 54, 411
Bahcall, J. N., & Loeb, A. 1990, ApJ, 360, 267
Bahcall, J. N., & Pinsonneault, M. H. 1992, Rev. Mod. Phys., 64, 885
———. 1995, Rev. Mod. Phys., 67, 781
Bahcall, J. N., Pinsonneault, M. H., Basu, S., & Christensen-Dalsgaard, J. 1997, Phys. Rev. Lett., 78, 171
Bahcall, J. N., & Ulrich, R. K. 1988, Rev. Mod. Phys., 60, 297
Barger, V., Deshpande, N., Pal, P. B., Phillips, R. J. N., & Whisnant, K. 1991, Phys. Rev. D, 43, 1759
Basu, S. 1998, MNRAS, 298, 719
Basu, S., & Antia, H. M. 1995, MNRAS, 276, 1402
———. 1997, MNRAS, 287, 189
Basu, S., Christensen-Dalsgaard, J., Hernandez, F. P., & Thompson, M. J. 1996, MNRAS, 280, 651
Basu, S., et al. 1997, MNRAS, 292, 243
———. 2000, ApJ, 535, 1078
Basu, S., Pinsonneault, M. H., & Bahcall, J. N. 2000, ApJ, 529, 1084 (BPB00)
Bellotti, E., et al. 2001, Nucl. Phys. B, 91, 44 (GNO Collaboration)
Berezinsky, V., Fiorentini, G., & Lissia, M. 1996, Phys. Lett. B, 365, 185
Bertello, L., et al. 2000a, ApJ, 535, 1066
Bertello, L., Varadi, F., Ulrich, R. K., Henney, C. J., Kosovichev, A. G., García, R. A., & Turck-Chièze, S. 2000b, ApJ, 537, L143
Brown, L. S., & Sawyer, R. F. 1997, ApJ, 489, 968
Brown, T. M., & Christensen-Dalsgaard, J. 1998, ApJ, 500, L195
Brun, A. S., Turck-Chièze, S., & Zahn, J. P. 1999, ApJ, 525, 1032
Canuto, V. J. 2000, ApJ, 534, L113
Castellani, V., Degl'Innocenti, S., Fiorentini, G., Lissia, M., & Ricci, B. 1997, Phys. Rep., 281, 309
Chaplin, W. J., et al. 1996, Sol. Phys., 168, 1
Christensen-Dalsgaard, J. 1988, in IAU Symp. 123, Advances in Helio- and Asteroseismology, ed. J. Christensen-Dalsgaard & S. Frandsen (Dordrecht: Reidel), 295
———. 1992, ApJ, 385, 354
———. 1995, in The Structure of the Sun, VI Canary Islands Winter School of Astrophysics, ed. T. Roca Cortés & F. Sánchez (Cambridge: Cambridge Univ. Press), 47
———. 1997, in IAU Symp. 185, New Eyes to See inside the Sun and Stars, ed. F. Deubner, J. Christensen-Dalsgaard, & D. Kurtz (Dordrecht: Kluwer), 245
Christensen-Dalsgaard, J., et al. 1996, Science, 272, 1286
Christensen-Dalsgaard, J., Gough, D. O., & Thompson, M. J. 1991, ApJ, 378, 413
Cleveland, B. T., Daily, T., Davis, R., Jr., Distel, J. R., Lande, K., Lee, C. K., Wildenhain, P. S., & Ullman, J. 1998, ApJ, 496, 505
Cox, A. N., Kidman, R. B., & Newman, M. J. 1985, in AIP Conf. Proc. 126, Solar Neutrinos and Neutrino Astronomy, ed. M. L. Cherry & W. A. Fowler (New York: AIP), 93
Crommelynck, D., Fichot, A., Domingo, V., & Lee, R., III 1996, Geophys. Res. Lett., 23, 2293
Cumming, A., & Haxton, W. C. 1996, Phys. Rev. Lett., 77, 4286
Davis, R. 1994, Prog. Part. Nucl. Phys., 32, 13
Davis, R., Jr., Harmer, D. S., & Hoffman, K. C. 1968, Phys. Rev. Lett., 20, 1205
Demarque, P., & Guenther, D. B. 1991, in Solar Interior and Atmosphere, ed. A. N. Cox, W. C. Livingston, & M. S. Matthews (Tucson: Univ. Arizona Press), 1186
Dzitko, H., Turck-Chièze, S., Delbourgo-Salvador, P., & Lagrange, C. 1995, ApJ, 447, 428
Ezer, D., & Cameron, A. G. W. 1968, ApJ, 1, L177
Fröhlich, C., & Lean, J. 1998, Geophys. Res. Lett., 25, 4377
Fukuda, Y., et al. 1996, Phys. Rev. Lett., 77, 1683 (Kamiokande Collaboration)
———. 1998, Phys. Rev. Lett., 81, 1158 (erratum, 81, 4279) (Super-Kamiokande Collaboration)
Gavrin, V. 2001, Nucl. Phys. B, 91, 36 (SAGE Collaboration)
Grevesse, N. 1984, Phys. Scr., 8, 49
Grevesse, N., & Noels, A. 1993, in Origin and Evolution of the Elements, ed. N. Prantzos, E. Vangioni-Flam, & M. Cassé (Cambridge: Cambridge Univ. Press), 15
Grevesse, N., & Sauval, A. J. 1998, Space Sci. Rev., 85, 161
Gruzinov, A. V., & Bahcall, J. N. 1997, ApJ, 490, 437
———. 1998, ApJ, 504, 996
Guenther, D. B. 1991, ApJ, 375, 352
Guenther, D. B., & Demarque, P. 1997, ApJ, 484, 937
———. 2000, ApJ, 531, 503
Guenther, D. B., Demarque, P., Kim, Y.-C., & Pinsonneault, M. H. 1992, ApJ, 387, 372
Guzik, J. A. 1998, in Proc. *SOHO* 6/GONG 98 Workshop, Structure and Dynamics of the Sun and Sun-like Stars, ed. S. G. Korzennik & A. Wilson (Noordwijk: ESA), 417
Guzik, J. A., & Cox, A. N. 1995, ApJ, 448, 905
Hampel, W., et al. 1999, Phys. Lett. B, 447, 127 (GALLEX Collaboration)
Iben, I., Jr. 1965, ApJ, 141, 933
———. 1967, ApJ, 147, 624
———. 1974, ARA&A, 12, 215
Iben, I., Jr., Kalata, K., & Schwartz, J. 1967, ApJ, 150, 1001
Iglesias, C. A., & Rogers, F. J. 1996, ApJ, 464, 943
Iglesias, C. A., Rogers, F. J., & Wilson, B. G. 1992, ApJ, 397, 717
Kurucz, R. L. 1991, in NATO ASI Ser., Stellar Atmospheres: Beyond Classical Models, ed. L. Crivellari, I. Hubeny, & D. G. Hummer (Dordrecht: Kluwer), 441
Lande, K. 2001, in Proc. of the XIX International Conf. on Neutrino Physics and Astrophysics (Amsterdam: Elsevier), in press
Leibacher, J. W., & Stein, R. F. 1971, ApJ, 7, L191
Lim, C. S., & Marciano, W. 1988, Phys. Rev. D, 37, 1368
Marcucci, L. E., Schiavilla, R., Viviani, M., Kievsky, A., & Rosati, S. 2000a, Phys. Rev. Lett., 84, 5959
Marcucci, L. E., Schiavilla, R., Viviani, M., Kievsky, A., Rosati, S., & Beacom, J. F. 2000b, Phys. Rev. C, 63, 015801
Merryfield, W. J. 1995, ApJ, 444, 318
Mikheyev, S. P., & Smirnov, A. Yu. 1985, Soviet J. Nucl. Phys., 42, 913
———. 1986, in Proc. of the 6th Moriond Workshop, 86 Massive Neutrinos in Astrophysics and in Particle Physics, ed. O. Fackler & Trân Thanh Vân (Gif-sur-Yvette: Editions Frontières), 355

Mitler, H. E. 1977, ApJ, 212, 513
Monteiro, M., Christensen-Dalsgaard, J., & Thompson, M. J. 2000, MNRAS, 316, 165
Morel, P., Pichon, B., Provost, J., & Berthomieu, G. 1999, A&A, 350, 275
Morel, P., Provost, J., & Berthomieu, G. 2000a, A&A, 353, 771
Morel, P., Provost, J., Lebreton, Y., Thévenin, F., & Berthomieu, G. 2000b, A&A, 363, 675
Pinsonneault, M. H. 1997, ARA&A, 35, 557
Pinsonneault, M. H., Steigman, G., Walker, T. P., & Narayanan, V. K. 1999, ApJ, 527, 180
Pontecorvo, B. 1968, Soviet Phys.-JETP, 26, 981
Proffitt, C. R. 1994, ApJ, 425, 849
Proffitt, C. R., & Michaud, G. 1991, ApJ, 380, 238
Rhodes, E. J., Jr., Kosovichev, A. G., Schou, J., Scherrer, P. H., & Reiter, J. 1997, Sol. Phys., 175, 287
Ricci, B., & Fiorentini, G. 2000, Nucl. Phys. B, 81, 95
Richard, O., Vauclair, S., Charbonnel, C., & Dziembowski, W. A. 1996, A&A, 312, 1000
Richer, J., Michaud, G., & Turcotte, S. 2000, ApJ, 529, 338
Rogers, F. J., Swenson, F. J., & Iglesias, C. A. 1996, ApJ, 456, 902
Salpeter, E. E. 1954, Australian J. Phys., 7, 373
Scherrer, P. H., Wilcox, J. M., Christensen-Dalsgaard, J., & Gough, D. O. 1983, Sol. Phys., 82, 75
Schou, J., Kosovichev, A. G., Goode, P. R., & Dziembowski, W. A. 1997, ApJ, 489, L197
Suzuki, Y. 2001, Nucl. Phys. B, 91, 29
Tassoul, M. 1980, ApJS, 43, 469
Thiery, S., et al. 2000, A&A, 355, 743
Thoul, A. A., Bahcall, J. N., & Loeb, A. 1994, ApJ, 421, 828
Tomczyk, S., Schou, J., & Thompson, M. J. 1995a, ApJ, 448, L47
Tomczyk, S., Streander, K., Card, G., Elmore, D., Hull, H., & Caccani, A. 1995b, Sol. Phys., 159, 1
Toutain, T., Appourchaux, T., Fröhlich, C., Kosovichev, A. G., Nigam, R., & Scherrer, P. H. 1998, ApJ, 506, L147
Turck Chièze, S., et al. 1997, Sol. Phys., 175, 247
———. 1998, in Proc. *SOHO* 6/GONG 98 Workshop: Structure and Dynamics of the Sun and Sun-like Stars, ed. S. G. Korzennik & A. Wilson (Noordwijk: ESA), 555
Turck Chièze, S., Vignaud, D., Däppen, W., Fossat, E., Provost, J., & Schatzman, E. 1993, Phys. Rep., 230, 57
Turcotte, S., & Christensen-Dalsgaard, J. 1998, Space Sci. Rev., 85, 133
Turcotte, S., Richer, J., Michaud, G., Iglesias, C. A., & Rogers, F. J. 1998, ApJ, 504, 539
Ulrich, R. K. 1970, ApJ, 162, 993
———. 1986, ApJ, 306, L37
Weiss, A., & Schlattl, H. 1998, A&A, 332, 215
Wolfenstein, L. 1978, Phys. Rev. D, 17, 2369